Nucleic Acids Research, 2025, **53**, gkaf130
https://doi.org/10.1093/nar/gkaf130
Gene regulation, Chromatin and Epigenetics

Rescuing DNMT1 fails to fully reverse the molecular and functional repercussions of its loss in mouse embryonic stem cells

Elizabeth Elder[1,2], Anthony Lemieux[1,2], Lisa-Marie Legault[1,2], Maxime Caron[3], Virginie Bertrand-Lehouillier[1,2], Thomas Dupas[2,4], Noël J-M. Raynal[2,5], Guillaume Bourque[6,7], Daniel Sinnett[2,8], Nicolas Gévry[9], Serge McGraw[1,2,4,*]

[1]Department of Biochemistry and Molecular Medicine, University of Montreal, Montreal, Quebec, H3T 1J4, Canada
[2]Azrieli Research Centre of Sainte-Justine University Hospital, Montreal, Quebec, H3T 1C5, Canada
[3]University of Montreal Hospital Research Centre, Montreal, Quebec, H2X 0A9, Canada
[4]Department of Obstetrics and Gynecology, University of Montreal, Montreal, Quebec, H3T 1J4, Canada
[5]Department of Pharmacology and Physiology, University of Montreal, Montreal, Quebec, H3T 1J4, Canada
[6]Department of Human Genetics, McGill University, Montreal, Quebec, H3A 1Y2, Canada
[7]McGill Genome Centre, Montreal, Quebec, H3A 0G1, Canada
[8]Department of Pediatrics, University of Montreal, Montreal, Quebec, H3T 1C5, Canada
[9]Department of Biology, University of Sherbrooke, Sherbrooke, Quebec, J1K 2R1, Canada

[*]To whom correspondence should be addressed. Email: serge.mcgraw@umontreal.ca

Abstract

Epigenetic mechanisms are crucial for developmental programming and can be disrupted by environmental stressors, increasing susceptibility to disease. This has sparked interest in therapies for restoring epigenetic balance, but it remains uncertain whether disordered epigenetic mechanisms can be fully corrected. Disruption of DNA methyltransferase 1 (DNMT1), responsible for DNA methylation maintenance, has particularly devastating biological consequences. Therefore, here we explored if rescuing DNMT1 activity is sufficient to reverse the effects of its loss utilizing mouse embryonic stem cells. However, only partial reversal could be achieved. Extensive changes in DNA methylation, histone modifications, and gene expression were detected, along with transposable element derepression and genomic instability. Reduction of cellular size, complexity, and proliferation rate were observed, as well as lasting effects in germ layer lineages and embryoid bodies. Interestingly, by analyzing the impact on imprinted regions, we uncovered 20 regions exhibiting imprinted-like signatures. Notably, while many permanent effects persisted throughout *Dnmt1* inactivation and rescue, others arose from the rescue intervention. Lastly, rescuing DNMT1 after differentiation initiation worsened outcomes, reinforcing the need for early intervention. Our findings highlight the far-reaching functions of DNMT1 and provide valuable perspectives on the repercussions of epigenetic perturbations during early development and the challenges of rescue interventions.

Graphical abstract

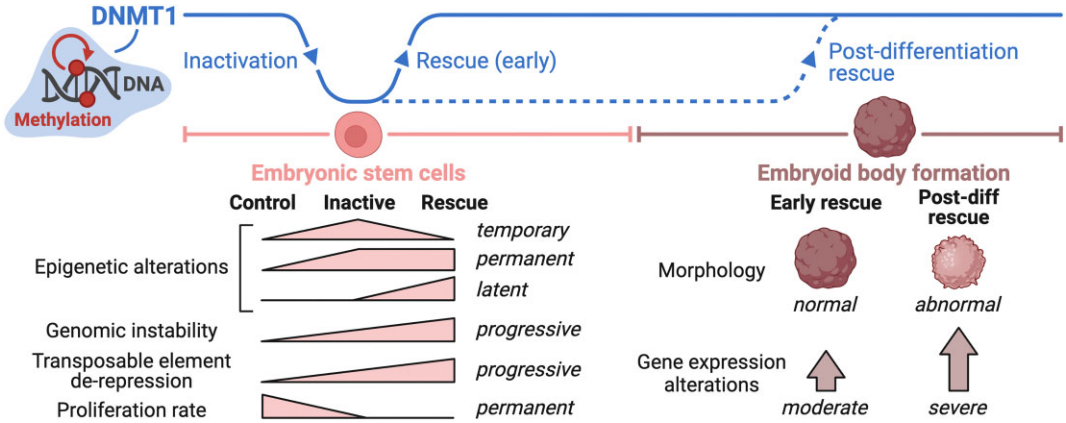

Received: May 24, 2024. **Revised:** December 27, 2024. **Editorial Decision:** February 6, 2025. **Accepted:** February 11, 2025

Introduction

Epigenetic mechanisms, including DNA methylation and histone modifications, play a fundamental role in developmental programming by regulating molecular and cellular processes in response to internal and external stimuli without altering the underlying DNA sequence [1–4]. Extensive research reveals that exposures to environmental stressors during development—such as toxins [5, 6], poor nutrition [7–9], alcohol [10–12], assisted reproductive technology [13–17], and psychological stress [18, 19]—can interfere with normal epigenetic programming, often with cell type [20–22] and sex [11, 23] related specificities, thereby increasing susceptibility to various diseases and health issues. This has sparked a growing interest in therapeutic interventions aimed at mitigating epigenetic disruptions to reinstate molecular and cellular homeostasis [24–28]. Yet, it remains uncertain if the detrimental impact of disordered epigenetic mechanisms can in fact be thoroughly remedied, all while avoiding potentially serious side effects.

DNA methyltransferase 1 (DNMT1) is a cornerstone of epigenetic regulation, primarily responsible for maintaining DNA methylation patterns during cellular division [29–32]. DNA methylation maintenance by DNMT1 ensures epigenetic stability across cell generations [33], playing a critical role in genome integrity [34], genomic imprinting [35–37], transposable element silencing [38, 39], gene expression regulation [40], and cell fate decisions [41–43]. DNMT1 levels are finely tuned to specific developmental contexts; for instance, they are elevated in stem and progenitor cells and decrease during specialized differentiation [44–47]. Aberrant DNMT1 activity—either deficiency or excess—disrupts DNA methylation profiles, leading to widespread hypomethylation [48–50] or localized hypermethylation [51–54], respectively. Beyond its catalytic function in DNA methylation, DNMT1 interacts with histone modifiers [55, 56], chromatin remodelers [57], and noncoding RNAs [58], exerting influence over broader epigenetic networks [59, 60]. Given the wide-ranging scope of its mechanisms, dysregulation of DNMT1 has severe biological consequences, leading to embryonic lethality in mice [51, 61] and contributing to the progression of various diseases such as developmental disorders [62], cancer [63, 64], schizophrenia [65, 66], and neurodegenerative pathologies [67–69]. Emerging strategies for correcting abnormal DNA methylation profiles show promise for the treatment of disease [69–72]. However, further research is needed to determine if DNA methylation perturbations can be rectified while fully reversing their effects on a broader molecular and cellular scale and without inflicting any collateral damage.

For mechanistic studies of epigenetic perturbations, embryonic stem cells (ESCs) serve as particularly useful models because of their pluripotency, rapid proliferation, relevance to both development and disease, and, importantly, their cellular plasticity [73–75]. Cellular plasticity is a key characteristic that enables ESCs to tolerate substantial epigenetic alterations, allowing for stable cell cultures with aberrant expression of epigenetic enzymes while remaining in a pluripotent state and maintaining proliferative capacity [36, 76–78]. To investigate the feasibility of reversing DNA methylation perturbations, *Dnmt1*$^{tet/tet}$ mouse ESCs (mESCs) [36] can be leveraged as a rescue model, wherein transient *Dnmt1* inactivation is achieved via the Tet-Off expression system [79], which facilitates reversible repression of an endogenous target gene with doxycycline treatment [79]. Due to typical transactivation effects of the Tet-Off system [80], *Dnmt1*$^{tet/tet}$ mESCs have higher DNMT1 levels relative to their wild-type counterpart; nevertheless, they function as a stable ESC line [36, 44, 81] capable of differentiating along early developmental trajectories, with their derived embryoid bodies exhibiting comparable morphology to those from wild-type mESCs [44]. The *Dnmt1*$^{tet/tet}$ mESC model is therefore well-suited to explore whether restoring DNMT1 activity is sufficient for reversing the impact of its loss or if long-term effects persist post-rescue. Indeed, we and others have employed *Dnmt1*$^{tet/tet}$ mESCs to demonstrate that loss of DNA methylation at imprinted regions is permanent when DNMT1-mediated DNA methylation maintenance is transiently interrupted [36, 37], and we further showed that other, nonimprinted regions throughout the genome also become permanently hypomethylated [37].

Recognizing DNMT1's far-reaching functions beyond DNA methylation maintenance, this study expands on our previous work to uncover the broader molecular and cellular alterations arising in *Dnmt1*$^{tet/tet}$ mESCs after inactivating and rescuing *Dnmt1*. We profiled DNA methylation with enhanced coverage and sensitivity, five key histone modifications (H3K4me3, H3K27ac, H3K4me1, H3K27me3, and H3K9me3), gene expression, transposable element silencing, genomic stability, as well as examined various cellular processes. Transient *Dnmt1* inactivation resulted in extensive epigenomic and gene expression alterations, derepression of transposable elements and genomic instability. Reduction of cell size, internal complexity, and proliferation rate were also detected, as well as lasting ramifications upon differentiation toward endoderm, mesoderm, and ectoderm germ layers and embryoid bodies. Moreover, analyzing the impact on known imprinted regions enabled the identification of 20 regions exhibiting imprinted-like epigenetic and regulatory signatures. Notably, while many permanent effects were observed throughout *Dnmt1* inactivation and rescue, others were triggered by the rescue intervention itself. Lastly, delaying *Dnmt1* rescue until after differentiation initiation led to worse outcomes, underscoring the importance of early intervention. Our findings provide foundational insights into the multifaceted mechanisms of DNMT1, emphasize the wide-ranging repercussions of epigenetic perturbations, and highlight the challenges associated with rescue interventions.

Materials and methods

Cell lines and culture protocol

R1 and *Dnmt1*$^{tet/tet}$ mESCs were gifted by Gregor Andelfinger (University of Montreal) and J. Richard Chaillet (University of Pittsburgh), respectively. Both cell lines were maintained on gelatin-coated plates, free of mouse embryonic fibroblast feeder cells, in mESC culture medium in humidified atmosphere with 5% CO_2 at 37°C. Cell culture plates were coated with 0.1% solution of gelatin (Sigma–Aldrich, G1890) in Dulbecco's Phosphate Buffered Saline (DPBS) 1× (Corning, 21-031-CV), then placed in the incubator for 30 min after which excess gelatin was removed. Culture medium for mESCs consisted of Dulbecco's modified Eagle medium (DMEM) (Corning, 10-013-CV) supplemented with 15% ESC-qualified fetal bovine serum (Thermo Fisher, 16141079), 1% 2-mercaptoethanol 100× (Sigma–Aldrich, ES-007-E), 1% nonessential amino acids 100× (Thermo Fisher, 11140050),

1% L-glutamine 200 mM (Corning, 25-005-CI), 1% nucleosides 100× (Sigma–Aldrich, ES-008-D), 1% penicillin–streptomycin 100× (Corning, 30-002-CI) and 10^3 U/ml of recombinant mouse leukemia inhibitory factor (LIF) (Sigma–Aldrich, ESG1107), which was stored at 4°C for up to 1 week. Culture medium was changed every day and cell confluency was maintained < 80%. Trypsin–EDTA 0.25% (Thermo Fisher, 25200056) was used for passaging cell cultures, typically every other day.

Dnmt1 inactivation and rescue in *Dnmt1*$^{tet/tet}$ mESCs

To inactivate *Dnmt1*, *Dnmt1*$^{tet/tet}$ mESCs were treated with 2 μg/ml doxycycline hyclate (Sigma–Aldrich, D9891), a tetracycline derivative, which was added to the culture medium for 6 days. Then, doxycycline treatment was stopped, and cells were maintained for 21 days. Samples were collected prior to doxycycline treatment (*Dnmt1*-control), immediately following doxycycline treatment (*Dnmt1*-inactive), and after the 21-day period of recovery from doxycycline treatment (*Dnmt1*-rescue).

Protein extraction

Cell pellets were resuspended in lysis buffer, consisting of radioimmunoprecipitation assay (RIPA) buffer with 1 mM phenylmethylsulfonyl fluoride (Bio Basics, PB0425), 0.25% Nonidet P-40 (BioShop, NON505), 1× Protease Inhibitor Cocktail (Roche, 11836170001), 20 mM EDTA pH 8.0 (Bio Basics, EB0185) and 1× PhosSTOP (Roche, 04906837001). The tubes were then gently shaken for 10 min at 4°C and centrifuged at 10 000 *g* for 5 min at 4°C, after which the supernatants were collected. Proteins were quantified using the Pierce BCA Protein Assay Kit (Thermo Fisher Scientific, 23227).

Western blot

Proteins were mixed with Laemmli buffer 5× and loaded into an acrylamide gel (stacking: 4%; resolving: 7%). Migration was performed for 10 min at 80 mV followed by 90 min at 120 mV until the 30 kDa molecular weight marker (Bio-Rad, 1610374) reached the bottom of the gel. Proteins were then transferred on a nitrocellulose membrane, which was saturated under soft agitation for 90 min at room temperature with 5% milk (BioShop, SKI400). The membrane was then incubated under soft agitation overnight at 4°C with the primary antibodies for DNMT1 (Cell Signaling Technology, 5032) and β-actin (Cell Signaling Technology, 4970) diluted at 1/1000 in 5% milk. The membrane was washed three times for 10 min in tris-buffered saline with 0.1% Tween® 20 (TBST) and incubated under soft agitation for 1 h at room temperature with the secondary antibody (anti-rabbit IgG HRP-linked; Cell Signaling Technology, 7074) diluted at 1/10 000 in 5% milk. The membrane was washed again three times for 10 min in TBST and revealed using the Clarity Western ECL substrate (Bio-Rad, 1705061) and the ChemiDoc Imaging System.

Genomic region annotations

Genomic coordinates for known imprinted regions were curated from literature [82–105], and sources specific to each region are listed in Supplementary Table S3. Allele-specific methylated regions in mESCs identified by the Smith Lab [106] in data from Leung *et al.* [107] were obtained via the UCSC table browser [108] from the DNA methylation Track Hub. Rsubread [109] v2.16.1 was used to obtain gene transcription start sites (TSS), TSS regions (±200 bp from TSS), promoters (−2000 and +200 bp from TSS), and gene bodies. Genomic regions not within promoters or gene bodies were considered as intergenic. Annotatr [110] v1.28.0 was used to obtain cytosine-phosphate-guanine (CpG) islands, CpG island shores (±2 kb from CpG islands), and CpG island shelves (±2 kb from CpG island shores). Genomic regions not within CpG islands, CpG island shores or CpG island shelves were considered as open sea. Using the UCSC table browser [108], candidate *cis*-regulatory elements (cCREs) bound by CCCTC-binding factor (CTCF) were extracted from the ENCODE Registry of cCREs [111] filtering for CTCF-only_CTCF-bound, PLS_CTCF-bound, dELS_CTCF-bound, pELS_CTCF-bound, and DNase-H3K4me3_CTCF-bound ENCODE classifications. Long interspersed nuclear elements (LINEs), short interspersed nuclear elements (SINEs), and long terminal repeats (LTRs) were extracted from RepeatMasker using the UCSC table browser [108]. The mouse reference genome assembly GRCm38/mm10 was used for all annotations.

Enzymatic methyl sequencing and data analysis

The following steps were performed in triplicates for each experimental condition: genomic DNA extraction using the QIAamp DNA Mini Kit (QIAGEN, 51304), library preparation using the NEBNext® Enzymatic Methyl-seq Kit (New England Biolabs, E7120L) and 150 bp paired-end sequencing using the Illumina NovaSeq 6000 technology. Library preparation and sequencing were conducted by *Génome Québec*. Between 291M and 385M raw reads were obtained per sample.

Raw reads were processed using the GenPipes [112] methylation sequencing pipeline v3.6.0. Trimmomatic [113] v0.36 was employed for quality trimming of raw reads and removal of sequencing adapters, Bismark [114] v0.18.1 for read alignment to the mouse reference genome assembly GRCm38/mm10, Sambamba [115] v0.7.0 for merging read set files of each sample, Picard v2.9.0 for removing duplicate reads, and the methylation extractor function from Bismark [114] v0.18.1 for obtaining the methylation level of single CpGs. Only CpGs that were sequenced in all samples with a coverage ≥ 10× were retained. Methylation levels of single CpGs were then averaged across triplicates.

CpGs were annotated to genomic regions of interest using annotatr [110] v1.28.0. Annotation to promoters was given priority over gene bodies, and CpG islands were prioritized over CpG island shores and shelves, with shores taking precedence over shelves. For annotation to transposable elements, only LINEs, SINEs, and LTRs with a Smith Waterman alignment score ≥ 1000 were considered. When conducting differential analysis among experimental conditions, we used a 20% change in methylation levels of single CpGs and a 10% change in mean methylation levels across a specific genomic region as thresholds for establishing significance. For comparisons involving groups of multiple CpGs or genomic regions, appropriate statistical testing was applied as described in the quantification and statistical analysis section.

Chromatin immunoprecipitation sequencing and data analysis

Chromatin immunoprecipitation (ChIP) sequencing was performed in duplicates for each histone modification per experimental condition, and one aliquot of nonimmunoprecipitated chromatin (i.e. input) was sequenced per experimental condition. First, cells were fixed with a solution consisting of 13% formaldehyde (Sigma–Aldrich, 47608) in DPBS (Corning, 21-031-CV) for 10 min at room temperature with gentle rocking. Then, cell and nuclei lysis was performed, and chromatin was purified and sonicated using buffers and protocols from the IDeal ChIP-Seq Histone Kit (Diagenode, C01010051). Sonication was conducted with the Bioruptor® Pico sonication device (Diagenode, B01060010) for 15 cycles (30 s ON/ 30 s OFF) to obtain DNA fragments between 150 and 400 bp. Next, chromatin was precleared via incubation with protein G Dynabeads™ (Thermo Fisher, 10009D) for 1 h at 4°C on a rotator, after which samples were placed on a magnetic rack and input aliquots were taken from the supernatant. ChIP was then conducted as follows. Precleared chromatin samples were incubated overnight at 4°C on a rotator with histone modification antibodies—either anti-H3K4me3 (Active Motif, 39159), anti-H3K27ac (Abcam, ab4729), anti-H3K4me1 (Cell Signaling Technology, 5326), anti-H3K27me3 (Sigma–Aldrich, 07-449), or anti-H3K9me3 (Abcam, ab8898)—in quantities recommended by the antibody manufacturer. Dynabeads™ were added to the chromatin–antibody mixtures and were incubated for an additional 2 h at 4°C on a rotator. Protein A Dynabeads™ (Thermo Fisher, 10001D) or protein G Dynabeads™ (Thermo Fisher, 10009D) were used depending on the antibody source. Washing, elution, de-crosslinking, and DNA purification were then conducted using the IDeal ChIP-Seq Histone Kit (Diagenode, C01010051). Finally, libraries were prepared with the KAPA HyperPrep Kit (Roche, KK8502), and 50 bp paired-end sequencing was performed at the McGill Genome Centre using the Illumina HiSeq® 2500 technology. Between 16M and 59M raw reads were obtained per sample.

Raw reads were processed using a homemade pipeline including Trimmomatic [113] v0.32 for quality trimming of raw reads and removal of sequencing adapters, Burrows-Wheeler Aligner [116] v0.6.1 for read alignment to the mouse reference genome assembly GRCm38/mm10, the MergeSamFiles.jar and MarkDuplicates.jar scripts from Picard v1.70 for merging read set files of each sample and removing duplicate reads, respectively, and the View function from SAMtools [117] v0.1.18 for filtering reads as to only retain those with a mapping quality (MAPQ) score ≥ 15. Then, peak calling was performed using MACS2 [118] v2.0.10 with Python v2.7.8, correcting background noise with input signals. Next, MACS2 outputs and BAM files converted to BED format (via the bamTobed function from BEDTools [119] v2.27) were used in the profile_bins function from MAnorm2_utils v1.0.0. The profile_bins function allowed for genomic regions of MACS2-called peaks to be merged into a common set of histone-modified regions across all samples for each histone modification, computing normalized signal enrichment within each region. Finally, MAnorm2 [120] v1.0.0 was employed for conducting differential analysis of enrichment signals between experimental conditions, providing a *P*-value and $\log_2$ fold change for each histone-modified region. Annotatr [110] v1.28.0 was used to overlap histone-modified regions with other genomic regions and for measuring histone modification RPKM levels within specific regions of interest. Visualization of RPKM signal enrichment within specific target regions in Fig. 6E was generated with ComplexHeatmap [121] v2.16.0 and EnrichedHeatmap [122] v1.30.0.

Mouse sperm and oocyte CpG methylation

Mouse sperm and oocyte CpG methylation profiles were produced by Wang *et al.* [123] and analyzed by the Smith Lab [106] using the mouse reference genome assembly GRCm38/mm10. These were obtained via the UCSC table browser [108] from the DNA methylation Track Hub and annotated to genomic regions of interest using annotatr [110] v1.28.0 after which mean sperm- and oocyte-specific levels were computed.

ZFP57 DNA-binding motif enrichment analysis

The ZFP57 DNA-binding motif MA1583.1 [124, 125] was obtained from the JASPAR database [126]. Enrichment analysis was conducted using the Simple Enrichment Analysis (SEA) tool from the MEME Suite [127] v5.5.5 with shuffled input sequences used as controls.

mRNA sequencing and data analysis

Messenger RNA (mRNA) sequencing was conducted in triplicates for all experimental conditions. RNA was extracted using the RNeasy Mini Kit (QIAGEN, 74104), libraries were prepared with the NEBNext® Ultra™ II Directional RNA Library Prep Kit (New England Biolabs, E7765) in conjunction with the NEBNext® Poly(A) mRNA Magnetic Isolation Module (New England Biolabs, E7490), and 100 bp paired-end sequencing was performed with the Illumina NovaSeq 6000 Technology. Library preparation and sequencing were conducted by *Génome Québec*. Between 27M and 53M raw reads were obtained per sample.

Raw reads were processed using the GenPipes [112] RNA sequencing pipeline v3.1.4. First, Trimmomatic [113] v0.36 was used for quality trimming of raw reads and removal of sequencing adapters, and STAR [128] v2.5.3a was used for aligning reads to the mouse reference genome assembly GRCm38/mm10. Then, several functions from Picard v2.9.0 were employed: MergeSamFiles for merging read alignment files of each sample, SortSam for sorting files by coordinate, and MarkDuplicates for identifying read duplicates. Next, the HTSeq_count function from HTSeq [129] v0.7.2 was used with Python v2.7.13 for calculating raw counts, and StringTie [130] v1.3.5 was used for transcript assembly. Finally, DESeq2 [131] v1.18.1 was used with R v3.4.3 for generating normalized counts and conducting differential gene expression analysis between experimental conditions, producing an adjusted *P*-value and $\log_2$ fold change for each gene.

RNA sequencing and data analysis for transposable elements

RNA sequencing was conducted in duplicates for all experimental conditions. The AllPrep DNA/RNA Mini Kit (QIAGEN, 80204) was used for RNA extraction and the TruSeq® Stranded Total RNA Library Prep Human/Mouse/Rat Kit (Illumina, 20020596) for library preparation. 75 bp paired-end sequencing was performed at the McGill Genome Centre with

the Illumina HiSeq® 4000 technology. Between 63M and 88M raw reads were obtained per sample.

Raw reads were processed using the GenPipes [112] RNA sequencing pipeline v3.1.4. First, Trimmomatic [113] v0.36 was used for quality trimming of raw reads and removal of sequencing adapters and then reads were aligned to the mouse reference genome assembly GRCm38/mm10 using STAR [128] v2.5.3a. Next, several functions from Picard v2.9.0 were employed including MergeSamFiles for merging read alignment files of each sample, SortSam for sorting files by coordinate, and MarkDuplicates for identifying read duplicates. Then, we incorporated the featureCounts [132] function from Subread [133] v2.0.6 to obtain raw counts corresponding to genomic regions of LINE, SINE, and LTR elements, extracted from RepeatMasker using the UCSC table browser [108]. Finally, we employed DESeq2 [131] v1.18.1 with R v3.4.3 to generate normalized counts for each element, which were then averaged across replicates.

LINEs, SINEs, and LTRs were then filtered based on their Smith Waterman alignment score, only retaining those with a score ≥ 1000 for downstream transcriptional analysis. When comparing total normalized counts of an element between experimental conditions, a $\log_2$ fold change ≤ 1 or ≥ 1 was used as a threshold for establishing significance. For comparisons involving grouped locus-specific normalized counts, appropriate statistical testing was applied as described in the quantification and statistical analysis section.

Gene set enrichment analysis

Gene set enrichment analysis (GSEA) was conducted with the enricher function from clusterProfiler [134] v4.8.2 using all gene sets available for Mus musculus in the Molecular Signatures Database [135, 136] which were extracted via the R package msigdbr v7.5.1. The following parameters were applied for the GSEA: Benjamini–Hochberg *P*-value adjustment, minimum gene set size of 10, and maximum gene set size of 1000.

Visualization of genomic signal tracks

Genomic signal tracks were generated with Gviz [137] v1.44.2. Signal tracks of experimental replicates were merged by computing their average signals within common 10 bp bins using the banCoverage function from deepTools [138] v3.5.2, with forward and reverse tracks for RNA-seq and mRNA-seq being priorly merged for each sample. Signal tracks for *Zfp57* WT and KO mESCs were produced by Shi *et al.* [139] (GSE123942) and for *Setdb1* WT and KO mESCs by Barral *et al.* [140] (GSE171749), which were obtained via the Gene Expression Omnibus [141, 142].

FACS assay for detecting γH2AX and assessing cell size and granularity

The H2AX phosphorylation (γH2AX) for fluorescence-activated cell sorting (FACS) kit (Sigma–Aldrich, 17-344) was used to prepare cell samples following the manufacturer's protocol for fixation, permeabilization, and staining. Triplicates of experimental conditions were stained for γH2AX, and one unstained control sample was included per condition. One DNA damage positive control sample stained for γH2AX was also included, which consisted of *Dnmt1*^{CTL} mESCs that were irradiated with 10 Gγ using a Faxitron® irradiator six days prior to sorting. Samples were sorted with the BD LSRFortessa™ Cell Analyzer (BD Biosciences) and data were processed with the BD FACSDiva™ software v8.0.2 to identify γH2AX-positive cells. Forward scatter area (FSC-A) and side-scatter area (SSC-A) measurements were used for filtering out apoptotic-like cells. FSC-A and SSC-A measurements of the live cell population were then used for comparing cell size and granularity, respectively, across experimental conditions.

Measuring relative telomere length by qPCR

Genomic DNA was extracted from *Dnmt1*$^{tet/tet}$ mESCs and R1 mESCs using the QIAamp DNA Mini Kit (QIAGEN, 51304). Quantitative polymerase chain reaction (qPCR) primer sequences for mouse telomeric and *Rplp0* (single-copy gene) DNA were obtained from Callicott and Womack [143] who adapted the protocol developed by Cawthon [144] for measuring relative telomere length in human samples. qPCR primers were ordered from Integrated DNA Technologies and evaluated using customary PCR techniques, including annealing temperature optimization and amplification efficiency assessment. qPCR assays were performed using a LightCycler® 480 instrument (Roche) and the SensiFAST™ SYBR® No-ROX Kit (Bioline, BIO-98005), following the kit's 3-step protocol for 30 cycles with an annealing temperature of 62°C. Telomeric and *Rplp0* DNA were amplified by qPCR in all *Dnmt1*$^{tet/tet}$ mESC conditions and in R1 mESCs, with eight replicates for each amplification to ensure reproducibility. For telomeric DNA amplifications, 0.2 ng of DNA was used and for *Rplp0* DNA amplifications, 2 ng of DNA was used. Relative telomere length was calculated for individual replicates of each *Dnmt1*$^{tet/tet}$ mESC condition with the delta-delta C_t method [145] as in the protocol by Cawthon, using *Rplp0* as the reference single-copy gene for normalization and R1 mESCs as the reference DNA sample for relativization. The average *Rplp0*C_t value for each condition was used for normalizing telomeric DNA C_t values, and the average normalized telomeric DNA C_t value in R1 mESCs was used to relativize normalized telomeric DNA C_t values in *Dnmt1*$^{tet/tet}$ mESCs.

1. Mouse telomeric DNA forward primer sequence: CGGTTTGTTTGGGTTTGGGTTTGGGTTTGGGT TTGGGTT
2. Mouse telomeric DNA reverse primer sequence: GGCTTGCCTTACCCTTACCCTTACCCTTACCC TTACCCT
3. Mouse *Rplp0* DNA forward primer sequence: ACTG-GTCTAGGACCCGAGAAG
4. Mouse *Rplp0* DNA reverse primer sequence: TCAATG-GTGCCTCTGGAGATT

Assessment of cell proliferation rate

The Incucyte® S3 Live-Cell Imaging and Analysis System and its associated software for data processing (Sartorius) were used to assess cell proliferation rate by measuring the increase in confluency over the course of 30 h. Cells were seeded in 6-well plates at a density of 50 000 cells/cm^2 in triplicates for all experimental conditions and confluency measurements were taken at 0, 6, 12, 18, 24, and 30 h.

Differentiation of mESCs towards endoderm, mesoderm, and ectoderm lineages

After thawing mESCs, they were passaged twice according to the mESC culture protocol. The day before beginning differentiation protocols, mESCs were passaged using TrypLE™ Express Enzyme 1× (Thermo Fisher, 12604021) supplemented with 10 μM ROCK Inhibitor Y-27632 (STEMCELL Technologies, 72302) for detachment, re-seeding them with a density of 30 000 cells/cm^2 in mESC culture medium in dishes coated with laminin from mouse Engelbreth–Holm–Swarm sarcoma (Roche, 11243217001). For laminin coating, 2.5 μg/cm^2 of laminin diluted in DMEM (Corning, 10-013-CV) was added to cell culture dishes in a minimal volume to coat entire dish surface, after which excess laminin was removed, and dishes were air dried for 45 min inside sterile cell culture hood. The next day, mESC cultures were rinsed twice with differentiation medium prior to starting differentiation protocols. Differentiations were conducted in triplicates for each experimental condition, maintaining cultures in humidified atmosphere with 5% CO_2 at 37°C without passaging. Differentiation cultures were rinsed twice daily with differentiation medium prior to adding differentiation treatments to remove dead cells as a fair amount of cell death was expected. Differentiation treatment mixtures were freshly prepared each day.

For endoderm differentiation, the differentiation medium consisted of Roswell Park Memorial Institute (RPMI) medium (Thermo Fisher, 11875093) supplemented with 10% KnockOut™ Serum Replacement (Thermo Fisher, 10828028), 2% B-27™ minus insulin 50× (Thermo Fisher, A1895601), 1.5% N-2-hydroxyethylpiperazine-N-2-ethane sulfonic acid (HEPES) buffer 1 M (Thermo Fisher, 15630106), 1% 2-mercaptoethanol 100× (Sigma–Aldrich, ES-007-E), 1% nonessential amino acids 100× (Thermo Fisher, 11140050), 1% L-glutamine, 200 mM (Corning, 25-005-CI), 1% nucleosides 100× (Sigma–Aldrich, ES-008-D), and 1% penicillin–streptomycin 100× (Corning, 30-002-CI). Cells were treated with 5 μM CHIR99021 (Sigma–Aldrich, SML1046) and 50 ng/ml Activin A (R&D Systems, 338-AC) for 1 day followed by 50 ng/ml Activin A and 100 nM LDN193189 (STEMCELL Technologies, 72147) for 2 days.

For mesoderm differentiation, the differentiation medium consisted of Eagle's minimum essential medium (EMEM) (Corning, 10009CV), 10% KnockOut™ Serum Replacement (Thermo Fisher, 10828028), 1% sodium pyruvate, 100 mM (Thermo Fisher, 11360070), 1% 2-mercaptoethanol 100× (Sigma–Aldrich, ES-007-E), 1% nonessential amino acids 100× (Thermo Fisher, 11140050), 1% L-glutamine, 200 mM (Corning, 25-005-CI), 1% nucleosides 100× (Sigma–Aldrich, ES-008-D), and 1% penicillin–streptomycin 100× (Corning, 30-002-CI). Cells were treated with 5 μM CHIR99021 (Sigma–Aldrich, SML1046) and 21 ng/ml bone morphogenetic protein 4 (BMP4) (R&D Systems, 5020-BP) for 3 days.

For ectoderm differentiation, the differentiation medium was the same as the mESC culture medium but without recombinant mouse LIF protein. Cells were treated with 1 μM retinoic acid (Sigma–Aldrich, R2625) for 3 days.

On the last day of differentiation protocols, differentiation cultures were sorted based on lineage-specific cell surface markers and viability using FACS. Differentiation cultures were rinsed twice with FACS buffer consisting of DPBS 1× (Corning, 21-031-CV) supplemented with 1% ESC-qualified fetal bovine serum (Thermo Fisher, 16141079). A minimal volume of FACS buffer was added to coat entire dish surface, and cells were dissociated into single-cell suspension with a cell scraper and gentle pipetting and were transferred to conical tubes. Primary antibodies for cell surface markers were added to cell suspensions in the amount recommended by the manufacturer followed by an incubation of 45 min at 4°C, gently mixing every 10 min. The primary antibodies used for endoderm, mesoderm, and ectoderm were anti-CXCR4 (R&D Systems, MAB21651), anti-CDH2 (R&D Systems, AF6426), and anti-NCAM1 (R&D Systems, AF2408), respectively. Cell suspensions were then rinsed twice with FACS buffer and resuspended in FACS buffer containing the fluorophore-conjugated secondary antibody in the amount recommended by the manufacturer followed by an incubation of 45 min at 4°C, gently mixing every 10 min. The secondary antibodies used for endoderm, mesoderm, and ectoderm were APC-conjugated anti-Rat IgG (R&D Systems, F0113), APC-conjugated anti-Sheep IgG (R&D Systems, F0127), and Alexa Fluor™ 488-conjugated anti-Goat IgG (Thermo Fisher, A11055), respectively. Cell suspensions were rinsed twice with FACS buffer and resuspended in FACS buffer at a density of 2M cells/100 μl. Samples were transferred to FACS tubes, adding 5 μl per sample of propidium iodide 10 μg/ml (Thermo Fisher, P1304MP), a viability indicator, which was used for sorting out dead cells. Cells were sorted with the BD FACSAria™ Fusion Flow Cytometer (BD Biosciences), and data were processed with the BD FACSDiva™ software v8.0.2. One unstained control sample per differentiation condition and one control sample of dead cells stained with propidium iodide were also sorted. The control sample of dead cells consisted of pooled differentiated cells heated at 65°C for 1 min in a digital dry bath and then incubated on ice for 1 min. After sorting, RNA was immediately extracted and stored at −80°C for subsequent mRNA sequencing.

Embryoid body formation

Dnmt1$^{tet/tet}$ mESCs (*Dnmt1*-control, *Dnmt1*-inactive, and *Dnmt1*-rescue conditions) were detached with TrypLE™ Express Enzyme 1× (Thermo Fisher, 12604021) supplemented with 10 μM ROCK Inhibitor Y-27632 (STEMCELL Technologies, 72302) and counted with a hemocytometer. mESCs were seeded into 96-well round bottom ultra-low attachment plates (Corning, 7007) at 1000 cells per well in 150 μl of culture medium, centrifuged at 100 *g* for 3 min, and left undisturbed for 2 days. The culture medium used for the first 2 days of embryoid body formation was the same as the mESC culture medium but without nucleosides and with 10 μM ROCK Inhibitor Y-27632. From day 2 to day 4, the embryoid body culture medium was the same as the mESC medium but without LIF and nucleosides. From day 4 to day 10, the embryoid body culture medium was the same as the mESC medium but without LIF and nucleosides and with DMEM/F12 (Thermo Fisher, 11330032) instead of DMEM. Culture medium was changed daily by replacing two-thirds with fresh medium. Doxycycline hyclate (2 μg/ml; Sigma–Aldrich, D9891) was added to the embryoid body culture medium from day 0 (seeding) to day 10 for the *Dnmt1*-inactive condition, or from day 0 to day 5 for the post-differentiation *Dnmt1*-rescue condition. For post-differentiation rescue of *Dnmt1*, embryoid bodies were

rinsed three times on day 5 with culture medium to remove doxycycline. Embryoid body formation thus included four experimental conditions: *Dnmt1*-control, *Dnmt1*-inactive, *Dnmt1*-rescue, and post-differentiation *Dnmt1*-rescue. Embryoid bodies ($n = 192$ per condition) were derived from the same *Dnmt1*$^{tet/tet}$ mESC culture. From day 2 to day 10 of embryoid body formation, daily bright-field microscopy images were taken of 20 embryoid bodies per condition with an EVOS M5000 Cell Imaging System (Thermo Fisher). These images were used for measuring embryoid body surface area and perimeter with ImageJ software v1.54g. Surface area was used as an indicator of size and circularity was determined by the formula $4\pi \times \text{Area}/\text{Perimeter}^2$. Embryoid bodies were harvested and pooled on days 5 and 10 for protein and RNA extractions for western blotting and mRNA sequencing.

Deconvolution of embryoid body mRNA sequencing data

Raw mRNA-seq counts of embryoid bodies were deconvoluted from single-cell RNA-seq data of mouse gastrulation embryos obtained from the R package MouseGastrulationData v1.18.0 [146], using only data from embryonic day 7.75 embryos and selecting only extraembryonic (ExE) endoderm, epiblast, primitive streak, rostral neurectoderm, and forebrain/midbrain/hindbrain cell types. Rostral neurectoderm and forebrain/midbrain/hindbrain cell types were combined into one cell type category that we named neuroectoderm. Technical artifacts were filtered out of the single-cell data by removing doublets and cells with stripped nuclei. The deconvolution was performed with the function music2_prop_t_statistics from the R package MuSiC v1.0.0 [147, 148] using default function settings.

Quantification and statistical analysis

Statistical tests for comparing grouped data were conducted in R v4.3.1 using functions from the stats R core package. To determine whether parametric or nonparametric statistical tests should be used, we first applied the Shapiro–Wilk test for normality using the shapiro.test function as well as Levene's test for homogeneity of variance using the leveneTest function. Parametric testing was conducted if both the Shapiro–Wilk and Levene's tests passed, whereas nonparametric testing was conducted if either one failed. For pairwise comparisons across more than two experimental conditions, parametric testing was performed using one-way ANOVA followed by Tukey's HSD test with *P*-value adjustment via the aov and TukeyHSD functions, and nonparametric testing was performed using the Kruskal–Wallis test followed by the Wilcoxon rank-sum test with Benjamini–Hochberg *P*-value adjustment via the kruskal.test and pairwise.wilcox.test functions. For comparing two groups of data, parametric testing was performed with Student's *t*-test using the t.test function, and nonparametric testing was performed with the Kruskal–Wallis test using the kruskal.test function. Pearson's chi-squared tests were performed with the chisq.test function and principal component analysis with the prcomp function. Differential quantification and statistical analyses of histone-modified regions using MAnorm2 and of gene expression using DESeq2 are described in their respective method details section.

Results

Inactivation and rescue of *Dnmt1* in mESCs induces extensive epigenomic alterations

Utilizing *Dnmt1*$^{tet/tet}$ mESCs [36], we previously revealed through reduced-representation bisulfite sequencing (RRBS) that loss of DNA methylation (i.e. CpG methylation) due to *Dnmt1* inactivation is not fully restored upon *Dnmt1* rescue [37]. However, RRBS can only capture ~10% of the total CpGs in the genome, with considerable bias toward CpG-dense promoter regions [149–153]. To achieve a comprehensive genome-wide view of DNA methylation alterations throughout *Dnmt1* inactivation and rescue, here we employed the *Dnmt1*$^{tet/tet}$ mESC model and performed enzymatic methyl sequencing (EM-seq) which provides vastly superior CpG coverage and methylation sensitivity. In this study, 15 349 152 CpGs (~73% of total CpGs) were sequenced with EM-seq compared to 1 422 634 CpGs (~7% of total CpGs) in our previous study with RRBS. We also conducted genome-wide ChIP sequencing (ChIP-seq) for five key histone modifications (permissive: H3K4me3, H3K27ac, and H3K4me1; repressive: H3K27me3 and H3K9me3) to investigate the broader impact on epigenomic landscapes. Herein, untreated *Dnmt1*$^{tet/tet}$ mESCs are referred to as *Dnmt1*-control (*Dnmt1*^{CTL}), those after *Dnmt1* inactivation by doxycycline treatment as *Dnmt1*-inactive (*Dnmt1*^{INV}), and those after rescuing *Dnmt1* through doxycycline removal as *Dnmt1*-rescue (*Dnmt1*^{RES}) (Fig. 1A). Successful inactivation and rescue of *Dnmt1* were confirmed by western blot (Supplementary Fig. S8A).

We first compared overall methylation levels of single CpGs in *Dnmt1*^{CTL}, *Dnmt1*^{INV}, and *Dnmt1*^{RES} conditions across various genomic location contexts, revealing a near-total depletion in *Dnmt1*^{INV} and a sustained decrease in *Dnmt1*^{RES} for all contexts (Fig. 1B). Permanent reduction in CpG methylation levels observed in *Dnmt1*^{RES} was particularly sizable for chromosome X (−17%), chromosome Y (−32%), imprinted regions (−27%), intergenic (−13%), open sea (−10%), LINEs (−21%), and LTRs (−13%), in contrast to other genomic location contexts (genome-wide: −9%, autosomes: −9%, promoters: −2%, gene bodies: −6%, CpG islands (CGI): −0.6%, CGI shores: −1%, CGI shelves: −4%, CTCF-bound candidate cCREs: −0.4%, SINEs: −5%). However, considering that CpGs in promoters, CpG islands, and CTCF-bound cCREs were mostly poorly methylated in *Dnmt1*^{CTL} (median level < 7%), the extent of their permanent hypomethylation may not be directly comparable to regions with initially highly methylated CpGs.

To explore genome-wide methylation dynamics of single CpGs throughout *Dnmt1* inactivation and rescue, we measured the change in methylation for each CpG in *Dnmt1*^{INV} versus *Dnmt1*^{CTL} (Fig. 1C) and in *Dnmt1*^{RES} versus *Dnmt1*^{CTL} (Fig. 1D). We characterized a methylation increase ≥ 20% as hypermethylated and a decrease ≥ 20% as hypomethylated; all other changes were considered as stably methylated. Each CpG was then categorized based on its methylation change (hypermethylated, hypomethylated, and stable) in *Dnmt1*^{INV} and *Dnmt1*^{RES}, revealing nine alteration patterns (Fig. 1E). Among these, temporary hypomethylation, permanent hypomethylation, and permanent stability of methylation were the most prevalent, comprising ~9.9 million, ~3.2 million, and ~2.1 million CpGs, respectively. Although permanent stability was prominent, those

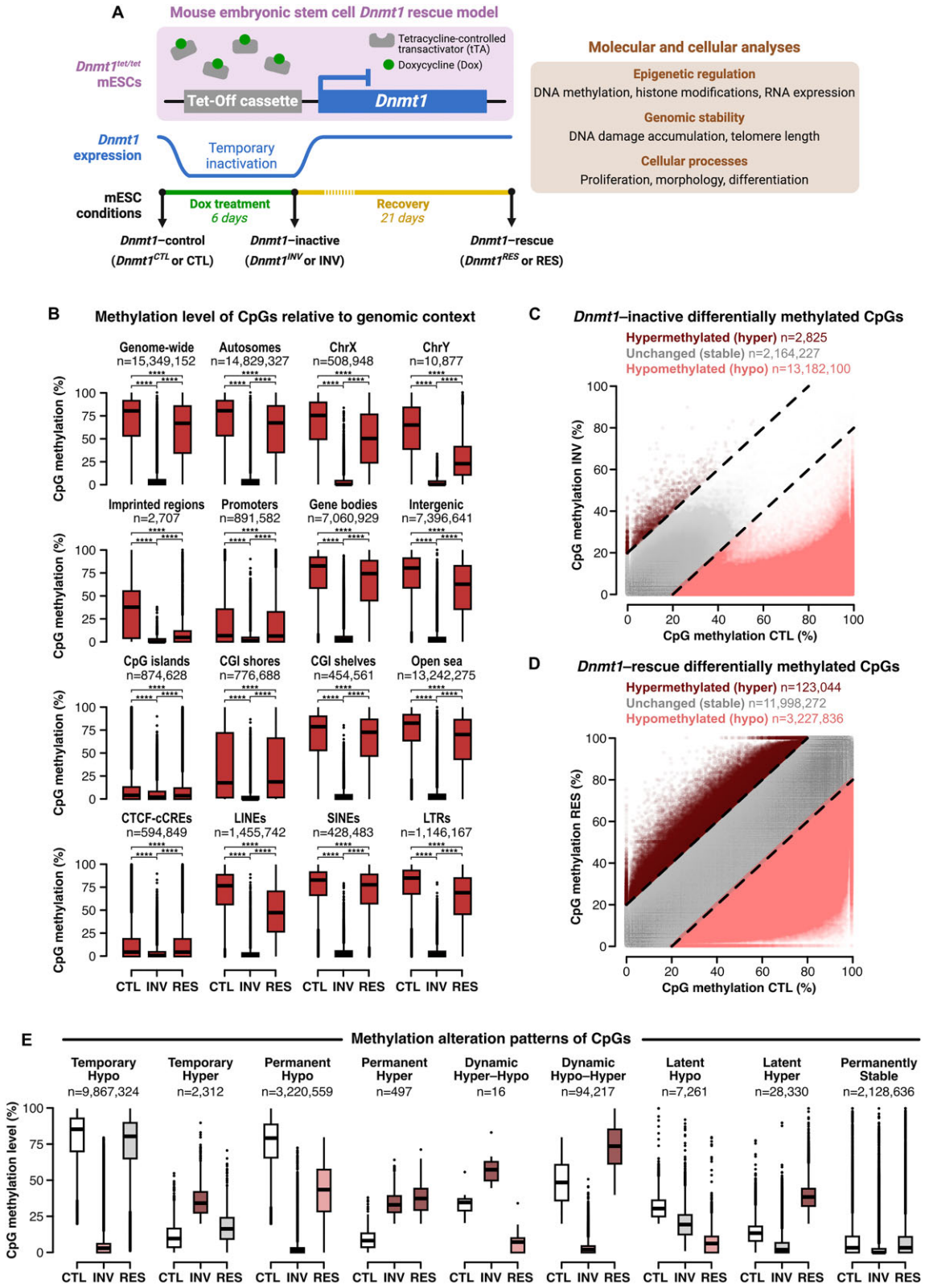

Figure 1. *Dnmt1* inactivation and rescue permanently reduces CpG methylation levels across genomic contexts, with over 3.2 million permanently hypomethylated single CpGs. (**A**) Schematic diagram depicting the *Dnmt1*$^{tet/tet}$ mESC model and molecular and cellular analyses performed. Created in BioRender: Dupas, T. (2025) https://BioRender.com/a16u385. (**B**) Pairwise comparisons of single CpG methylation levels in *Dnmt1*$^{\mathbf{CTL}}$, *Dnmt1*$^{\mathbf{INV}}$, and *Dnmt1*$^{\mathbf{RES}}$ (EM-seq: $n = 3$ per condition) relative to genomic location using the Wilcoxon rank sum test with Benjamini–Hochberg *P*-value adjustment. **** *P*-value ≤ 0.0001. (**C** and **D**) Differential methylation levels of genome-wide single CpGs in *Dnmt1*$^{\mathbf{INV}}$ and *Dnmt1*$^{\mathbf{RES}}$ versus *Dnmt1*$^{\mathbf{CTL}}$. Hypermethylated: increase $\geq 20\%$. Hypomethylated: decrease $\geq 20\%$. (**E**) Methylation alteration patterns of single CpGs during *Dnmt1* inactivation and rescue determined by differential states in panels (C) and (D). Temporary: hypo/hyper in *Dnmt1*$^{\mathbf{INV}}$ and stable in *Dnmt1*$^{\mathbf{RES}}$. Permanent: hypo/hyper in both *Dnmt1*$^{\mathbf{INV}}$ and *Dnmt1*$^{\mathbf{RES}}$. Dynamic: hypo/hyper in *Dnmt1*$^{\mathbf{INV}}$ and the opposite in *Dnmt1*$^{\mathbf{RES}}$. Latent: stable in *Dnmt1*$^{\mathbf{INV}}$ and hypo/hyper in *Dnmt1*$^{\mathbf{RES}}$. Permanently stable: stable in both *Dnmt1*$^{\mathbf{INV}}$ and *Dnmt1*$^{\mathbf{RES}}$. See also Supplementary Fig. S8A.

CpGs were mostly poorly methylated in $Dnmt1^{CTL}$ (median level < 3.4%), indicating limited potential for hypomethylation, unlike temporarily or permanently hypomethylated CpGs which were mostly highly methylated in $Dnmt1^{CTL}$ (median level > 85% and > 79%, respectively). Some CpG hypermethylation was observed, primarily in a dynamic hypo–hyper pattern ($n = 94\,217$) or a latent hypermethylation pattern ($n = 28\,330$). The remaining five patterns (temporary hyper, permanent hyper, dynamic hyper–hypo, and latent hypo) contained a negligible number of CpGs, totaling ~10K.

Next, we investigated the impact of *Dnmt1* inactivation and rescue in mESCs on histone modification landscapes. We first performed peak calling for H3K4me3, H3K27ac, H3K4me1, H3K27me3, and H3K9me3 in each condition. Compared to $Dnmt1^{CTL}$, the total number of peaks was higher in $Dnmt1^{INV}$ for all modifications, while lower peak numbers were observed in $Dnmt1^{RES}$, except for H3K4me3 which remained higher (Supplementary Fig. S1A). Recognizing that peak numbers alone may not fully capture fluctuations in histone modification levels due to variable peak size and enrichment, peak genomic regions across experimental conditions were merged into a common set of regions for each histone modification while also conducting signal enrichment normalization. This enabled statistical and quantitative comparisons between experimental conditions for detecting differentially histone-modified regions (DHMs). DHMs exhibiting either a decrease or an increase in histone modification enrichment, and regions that maintained stable enrichment were computed in $Dnmt1^{INV}$ (Fig. 2A) and in $Dnmt1^{RES}$ (Fig. 2B) versus $Dnmt1^{CTL}$. Subsequently, histone-modified regions were classified based on their differential states (decrease, increase, or stable) in both $Dnmt1^{INV}$ and $Dnmt1^{RES}$ conditions, revealing temporary, permanent, dynamic and latent histone modification alteration patterns (Fig. 2C and Supplementary Fig. S1B). Although most regions displayed permanent stability of histone modification enrichment (Supplementary Fig. S1B), thousands of DHMs were detected in $Dnmt1^{INV}$ and $Dnmt1^{RES}$ (Fig. 2A and B), with H3K4me3 increase in $Dnmt1^{INV}$ being the most striking. Interestingly, DHMs were predominantly condition-specific; the majority of DHMs in $Dnmt1^{INV}$ exhibited temporary alteration (Fig. 2D) and in $Dnmt1^{RES}$ showed latent alteration (Fig. 2E).

In summary, DNA methylation and histone modification landscapes were extensively altered throughout *Dnmt1* inactivation and rescue, showing that the effects of transient loss of DNMT1 activity extends beyond DNA methylation to affect broader epigenomic networks. This reveals the critical role of sustained DNA methylation maintenance for preserving epigenomic integrity across multiple layers, emphasizing the importance of considering wider epigenomic contexts when key epigenetic mechanisms are disrupted. Although most alterations triggered by *Dnmt1* inactivation were reversed upon rescue, many alterations persisted, and additional alterations emerged post-rescue, illustrating the challenges associated with fully rescuing epigenetic perturbations without collateral effects.

Permanent CpG hypomethylation is associated with specific genomic location contexts and histone modification alteration patterns

Dnmt1 inactivation and rescue permanently reduced DNA methylation levels of over 3.2 million CpGs. To elucidate underlying factors, we examined whether specific genomic contexts or certain histone modification alteration patterns were more or less associated with permanent hypomethylation of these CpG sites.

First, we computed the number of CpGs with the potential to undergo permanent hypomethylation, i.e. a sustained methylation decrease of at least 20% throughout $Dnmt1^{INV}$ and $Dnmt1^{RES}$. These CpGs had to exhibit a methylation level exceeding 20% in the $Dnmt1^{CTL}$ condition and were designated as methylated CpGs (mCpGs). The frequency of mCpGs (ratio of mCpGs to sequenced CpGs) was high (≥ 0.65) across most genomic contexts, except for promoters (0.33) and CGI shores (0.49), which exhibited moderate frequencies, and CpG islands (0.15) and CTCF-bound cCREs (0.24), for which frequencies were markedly low (Supplementary Fig. S2A and Supplementary Table S1). As for histone modification alteration patterns, H3K4me1 and H3K9me3 patterns exhibited high mCpG frequencies overall, while H3K4me3, H3K27ac and H3K27me3 patterns had variable mCpG frequencies (Supplementary Fig. S2B and Supplementary Table S2). Next, we quantified the number of permanently hypomethylated CpGs and their frequency (ratio of permanently hypomethylated CpGs to mCpGs) (Fig. 3A and C; and Supplementary Tables S1 and S2). This was followed by the application of Pearson's chi-squared test to discern positive, negative, or neutral association of permanent CpG hypomethylation with genomic location contexts (Fig. 3B and Supplementary Table S1) or with histone modification alteration patterns (Fig. 3D and Supplementary Table S2). Positive associations were observed for imprinted regions, sex chromosomes, LINEs, LTRs, intergenic, and open sea genomic location contexts. All H3K9me3 patterns, except dynamic increase–decrease, also exhibited positive association along with permanent and latent increase patterns of H3K4me3 and H3K27me3. While the permanent increase pattern of H3K27ac displayed neutral association, it approached significance for positive association. It is noteworthy that, despite having high mCpG frequencies in $Dnmt1^{CTL}$, certain genomic location contexts (e.g. gene bodies, CGI shelves, and SINEs) and histone modification alteration patterns (e.g. latent decrease of H3K4me3, temporary increase of H3K4me1, H3K27ac, or H3K27me3) were negatively associated with permanent CpG hypomethylation.

In brief, specific genomic contexts, including imprinted regions, LINEs, LTRs, and sex chromosomes were more susceptible to permanent CpG hypomethylation during *Dnmt1* inactivation and rescue. These results reinforce the necessity of sustained DNMT1 activity to ensure the heritability of DNA methylation at imprinted loci [36, 37] and suggest that other nonimprinted regions may possess heritable DNA methylation marks, validating findings from our previous study using RRBS [37]. Additionally, permanent CpG hypomethylation being positively associated with sex chromosomes could relate to how epigenetic perturbations often result in sex-specific consequences [11, 23]. Specific patterns of histone modification alterations, particularly H3K9me3, were also positively associated, suggesting that permanent loss of DNA methylation involved additional changes to the chromatin microenvironment. Therefore, simply reinstating DNA methylation maintenance is possibly insufficient to restore DNA methylation levels in some regions; concurrent targeting of histone modifications may be required to fully rescue epigenetic states.

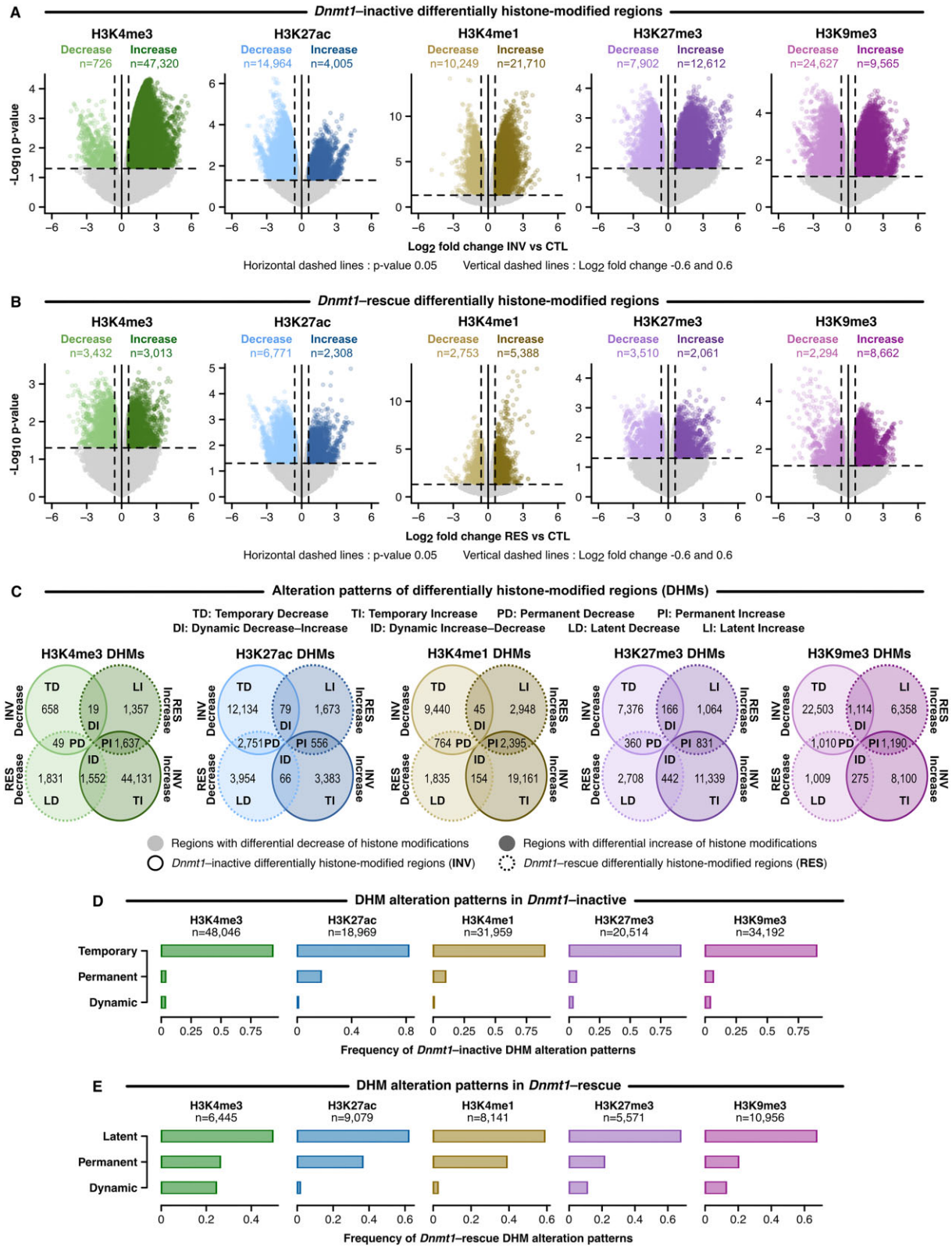

Figure 2. *Dnmt1* inactivation and rescue in mESCs alters genome-wide histone modification landscapes. (**A** and **B**) DHMs for H3K4me3, H3K27ac, H3K4me1, H3K27me3, and H3K9me3 in $Dnmt1^{INV}$ and $Dnmt1^{RES}$ versus $Dnmt1^{CTL}$ measured by ChIP-seq ($n = 2$ per condition) and determined by a *P*-value ≤ 0.05 and $\log_2$ fold change ≤ -0.6 or ≥ 0.6 using the MAnorm2 software. (**C**) Alteration patterns of DHMs for each histone modification throughout *Dnmt1* inactivation and rescue determined by their differential state in panels (A) and (B). Temporary: decrease/increase in $Dnmt1^{INV}$ and stable in $Dnmt1^{RES}$. Permanent: decrease/increase in both $Dnmt1^{INV}$ and $Dnmt1^{RES}$. Dynamic: decrease/increase in $Dnmt1^{INV}$ and the opposite in $Dnmt1^{RES}$. Latent: stable in $Dnmt1^{INV}$ and decrease/increase in $Dnmt1^{RES}$. (**D** and **E**) Frequency of DHM alteration patterns for $Dnmt1^{INV}$ and $Dnmt1^{RES}$, respectively, representing the number of DHMs in each pattern divided by the total number of DHMs. See also Supplementary Fig. S1.

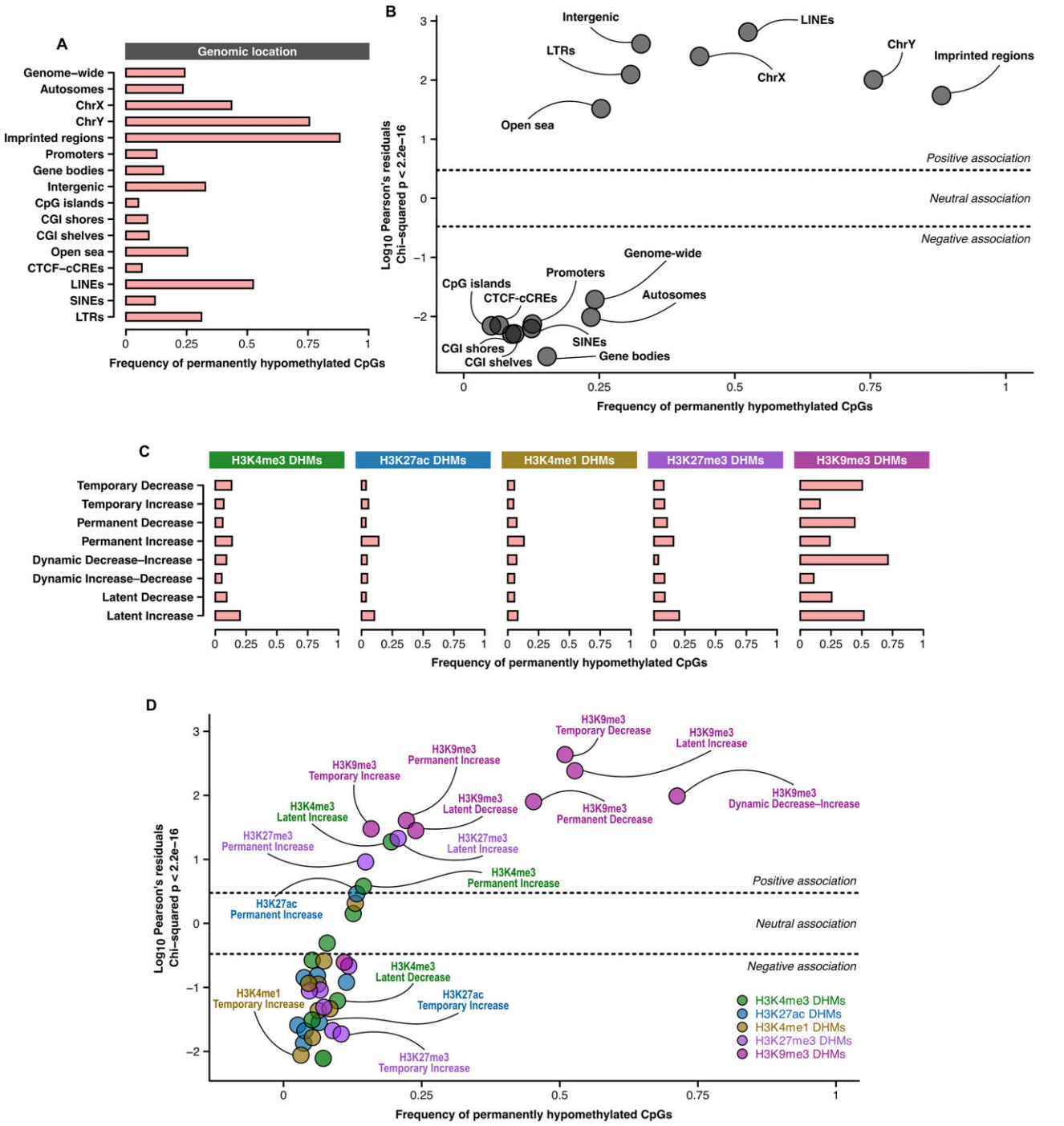

Figure 3. Permanent CpG hypomethylation is associated with specific genomic location contexts and histone modification alteration patterns. (**A**) Frequency of permanently hypomethylated CpGs per genomic location context. (**B**) Pearson's chi-squared test associating the frequency of permanently hypomethylated CpGs with genomic location contexts. (**C**) Frequency of permanently hypomethylated CpGs in DHMs categorized into alteration patterns identified in Fig. 2C. (**D**) Pearson's chi-squared test associating the frequency of permanently hypomethylated CpGs with DHM alteration patterns. Frequency of permanently hypomethylated CpGs represents the number of permanently hypomethylated CpGs divided by the number of methylated (methylation level $\geq$ 20%) CpGs in *Dnmt1*^{CTL}. Pearson's residual $\geq$ 2 indicates positive, $<$ 2 but $>$ −2 indicates neutral and $\leq$ −2 indicates negative association. See also Supplementary Tables S1 and S2 and Supplementary Fig. S2.

Analysis of known imprinted regions enables the identification of 20 regions with imprinted-like epigenetic and regulatory signatures

Genomic imprinting is an epigenetic phenomenon whereby certain genes are expressed in a parent-of-origin manner [154]. Epigenetic disruptions can cause failure of genomic imprinting maintenance, leading to severe developmental disorders [155, 156]. Imprinted regions are CpG-dense long-range *cis*-acting regulatory sites characterized by heritable allele-specific DNA methylation, maintained by the concerted actions of DNMT1, ZFP57, TRIM28, and SETDB1-mediated deposition of broad H3K9me3 domains [35–37, 107, 139, 154, 157, 158]. Although genomic imprinting remains an active field of research, its heritability mechanisms are not fully understood, and the search for novel imprinted regions is still ongoing. Here, we leveraged *Dnmt1*$^{tet/tet}$ mESCs to better understand how histone modifications contribute to genomic imprinting heritability and uncover other regions with imprinted signatures.

Among the 26 imprinted regions [82–105] that were examined, 15 had permanently hypomethylated CpGs, exhibited permanent mean CpG hypomethylation ≥ 10% and overlapped permanently decreased H3K9me3 regions (Fig. 2C), specifically within broad H3K9me3 domains (≥ 3000 bp) (Fig. 4A and Supplementary Table S3). The remaining 11 did not meet those criteria in addition to having low mCpG frequencies (≤ 0.25) and low mean CpG methylation levels in *Dnmt1*^{CTL} (median < 4%), thus were excluded from further analysis. To identify regions with imprinted-like signatures, we employed publicly available mESC allele-specific methylated regions identified by the Smith Lab [106] in data from Leung *et al.* [107]. We filtered allele-specific methylated regions based on their nonoverlap with known imprinted regions and on them exhibiting epigenetic dynamics akin to those observed in the 15 known imprinted regions selected in Fig. 4A: the presence of permanently hypomethylated CpGs, permanent mean CpG hypomethylation ≥ 10%, and overlapping permanently decreased H3K9me3 regions within broad domains ≥ 3000 bp. Ultimately, 20 imprinted-like regions were retained, named according to their intersection with or proximity to genes (Fig. 4B and Supplementary Table S3). In recent work by Yang *et al.* [159], genomic regions with imprinted signatures were identified in mouse preimplantation embryos through allele-specific profiling of DNA methylation and H3K9me3 alongside global depletion of H3K9me3 to establish mechanistic co-dependency. Their analysis unveiled 22 imprinted-like regions and performed Cas9-mediated deletions of five of them, demonstrating their importance for mouse development. Compellingly, three of our imprinted-like regions—*Spred2*, *Lipt1-Mitd1*, and *Zfp668*—coincided with imprinted-like regions identified by Yang *et al.* (Supplementary Fig. S3A), with *Lipt1-Mitd1* among the five that were confirmed biologically relevant.

In comparison to the selected 15 known imprinted regions, imprinted-like regions also had high frequencies of mCpGs in *Dnmt1*^{CTL} and high frequencies of permanently hypomethylated CpGs (Supplementary Fig. S3B), along with comparable mean CpG methylation levels in *Dnmt1*^{CTL} (Supplementary Fig. S3C). However, imprinted-like regions displayed lower CpG density (Supplementary Fig. S3D) and less severe permanent mean CpG hypomethylation (Supplementary Fig. S3E) than the selected 15 known imprinted regions. Next, we computed mean histone modification RPKM levels within each region in *Dnmt1*^{CTL}, *Dnmt1*^{INV}, and *Dnmt1*^{RES} (Supplementary Table S3), employing *z*-score normalization to reveal epigenetic alteration dynamics other than permanent CpG hypomethylation and H3K9me3 decrease (Fig. 4C). Notably prevalent among known imprinted regions and imprinted-like regions were a temporary sharp elevation in H3K4me3 levels and permanently higher levels of H3K4me1, with variable fluctuations in H3K27ac and H3K27me3 levels.

We then measured mean CpG methylation levels of each region in mouse oocytes and sperm using data from Wang *et al.* [123] analyzed by the Smith Lab [106] to explore germline inheritance of allele-specific CpG methylation in imprinted-like regions (Supplementary Table S3). Known imprinted regions exhibited anticipated oocyte- or sperm-specific CpG methylation, with the *Meg3* imprinted region having similar levels in oocyte and sperm as it acquires its imprinted status during development (Fig. 4D). Differential CpG methylation between gametes was also observed in imprinted-like regions (Fig. 4E); for instance, *Repin1* and *Errfi1* downstream showed oocyte specificity. Displaying gamete and mESC epigenetic profiles of *Repin1* and *Errfi1* downstream imprinted-like regions alongside those of oocyte-specific known imprinted regions *Mest* and *Plagl1* clearly showcased CpG hypermethylation in oocytes versus sperm and similar epigenetic alteration dynamics during *Dnmt1* inactivation and rescue in mESCs, especially for CpG methylation, H3K4me3, H3K4me1, and H3K9me3 (Supplementary Fig. S3F). While the distinction of gamete-specific CpG methylation in imprinted-like regions was generally less pronounced compared to known imprinted regions, they all exhibited substantial levels (> 35%) in at least one gamete (Fig. 4D and E, and Supplementary Table S3). This suggests germline inheritance of CpG methylation profiles, albeit not in an allele-specific manner for all imprinted-like regions. Allele specificity may be acquired postfertilization for some imprinted-like regions, as is the case for the *Meg3* imprinted region.

To further investigate regulation of imprinted-like regions by genomic imprinting mechanisms, we conducted enrichment analysis of ZFP57 DNA-binding motif (Fig. 4F), revealing positive matches with 80% of imprinted-like regions and, predictably, with 100% of known imprinted regions (Fig. 4G). Moreover, the permanent decrease of broad H3K9me3 detected in our model was strikingly mirrored in *Zfp57* KO mESCs [139] and *Setdb1* KO mESCs [140] for known imprinted regions (e.g. *H19*, *Peg13–Trappc9*, and *Zrsr1–Commd1*) and imprinted-like regions (e.g. *Zfp13*, *Rnf216 upstream*, and *Zf668*), with binding of ZFP57 and SETDB1 coinciding within these regions (Fig. 4H). This was observed regardless of gamete-specific CpG methylation, as evidenced by the *Zfp668* imprinted-like region displaying nearly identical profiles in both gametes.

Finally, we examined significant gene expression dysregulation (adjusted *P*-value ≤ 0.05) in *Dnmt1*^{INV} and *Dnmt1*^{RES} versus *Dnmt1*^{CTL} for imprinted genes controlled by the selected 15 known imprinted regions (Supplementary Fig. S4A and B, and Supplementary Table S4) and for genes associated with imprinted-like regions (Supplementary Fig. S4C and D, and Supplementary Table S4). As expected, numerous imprinted genes showed significant permanent downregulation (e.g. *Igf2*, *Trappc9*, *Cdkn1c*, and *Phlda2*) or upregulation (e.g. *Mest*, *Plagl1*, *H19*, and *Zrsr1*), mostly exhibiting strong dysregulation ($\log_2$ fold change ≤ −0.6 or ≥ 0.6).

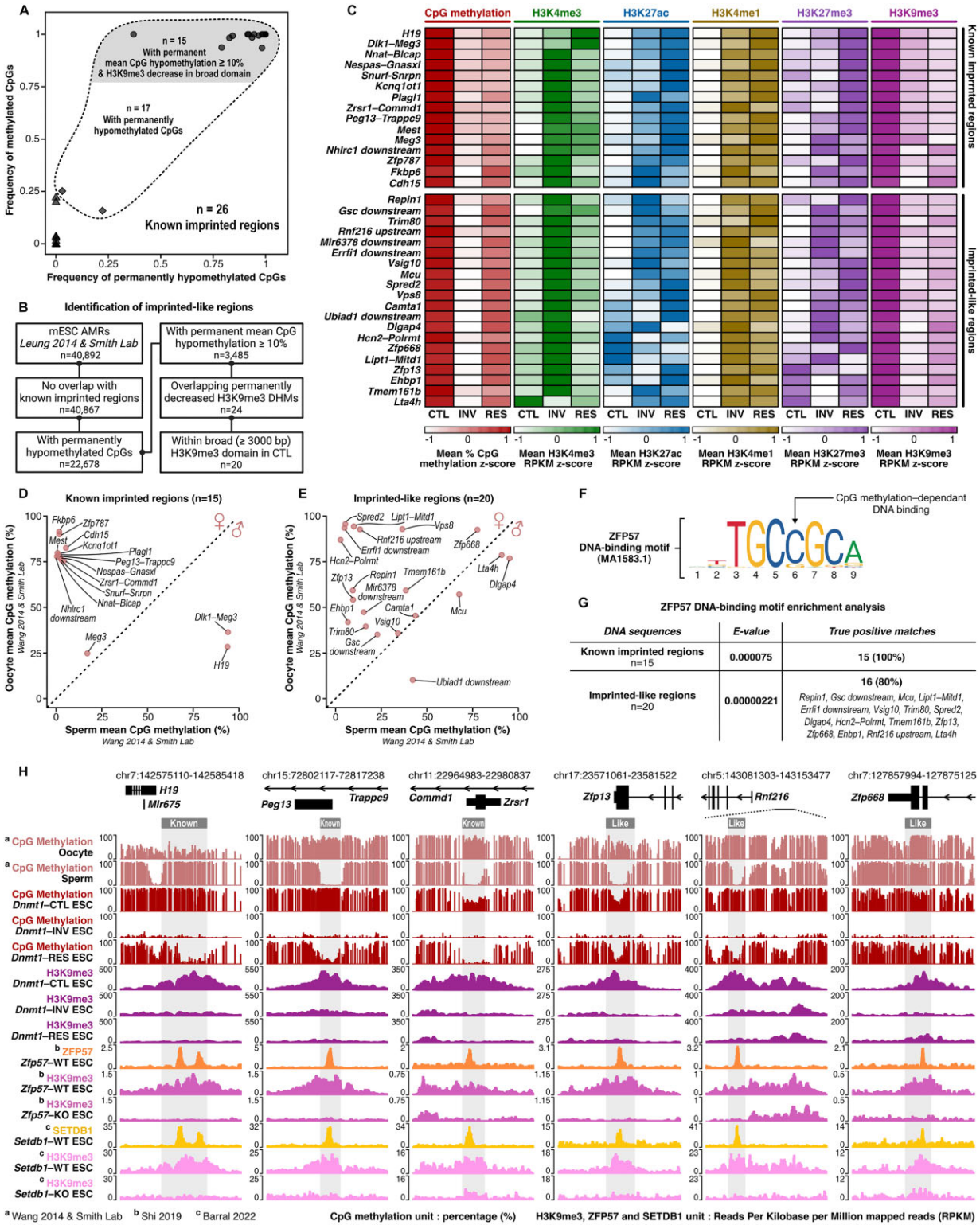

Figure 4. Analysis of known imprinted regions enables the identification of 20 regions with imprinted-like epigenetic and regulatory signatures. (**A**) Selection of 15 known imprinted regions based on four criteria: permanently hypomethylated CpGs ≥ 1, permanent mean CpG hypomethylation ≥ 10%, overlapping permanently decreased H3K9me3 DHMs, and located within H3K9me3 broad domains (≥ 3000 bp) in *Dnmt1*^{CTL}. (**B**) Workflow for identifying imprinted-like regions among mESC allele-specific methylated regions based on the four criteria in panel (A). Created in BioRender: Dupas, T. (2025) https://BioRender.com/r69z354. (**C**) Z-score normalization of epigenetic modification levels in *Dnmt1*^{CTL}, *Dnmt1*^{INV}, and *Dnmt1*^{RES} for selected known imprinted regions and imprinted-like regions. (**D** and **E**) Mean CpG methylation levels in oocytes versus sperm for selected known imprinted regions and imprinted-like regions, respectively. (**F**) ZFP57 DNA binding motif MA1583.1. (**G**) Enrichment of ZFP57 DNA binding motif MA1583.1 in selected known imprinted regions and imprinted-like regions. (**H**) Genomic signal tracks for *H19*, *Peg13–Trappc9*, and *Zrsr1–Commd1* imprinted regions and *Zfp13*, *Rnf216 upstream*, and *Zfp668* imprinted-like regions showing CpG methylation in gametes and *Dnmt1*$^{tet/tet}$ mESCs, H3K9me3 in *Dnmt1*$^{tet/tet}$ mESCs, *Zfp57* WT and KO mESCs and *Setdb1* WT and KO mESCs, ZFP57 binding in *Zfp57* WT mESCs, and SETDB1 binding in *Setdb1* WT mESCs. *See also* Supplementary Table S3 and Supplementary Fig. S3 and S4.

Some genes associated with imprinted-like regions were also significantly permanently downregulated (*Zfp668*) or upregulated (*Repin1*, *Rnf216*, *Hcn2*, and *Vsig10*), albeit with milder dysregulation. Nevertheless, 17 out of the 22 genes associated with imprinted-like regions were dysregulated in $Dnmt1^{INV}$, possibly suggesting a transcriptional impact linked to derepression of their imprinted-like region. However, given that imprinted-like regions are located outside gene promoters (Supplementary Table S3) and exhibit fluctuations in enhancer-associated marks H3K4me1 and H3K27ac, their regulatory target genes may be positioned at more distal locations. Directly assessing their influence on gene expression regulation would require a targeted derepression approach, such as DNA demethylation via clustered regularly interspaced short palindromic repeats (CRISPR)/dead CRISPR-associated protein 9 (dCas9)-based systems.

To summarize, our results suggest that, beyond H3K9me3, other histone modifications, notably enhancer-associated H3K4me1, play a role in the heritability of DNA methylation at imprinted loci. Our analyses also led to the identification of 20 imprinted-like regions exhibiting epigenetic and regulatory features closely resembling those of known imprinted regions. Interestingly, three imprinted-like regions (i.e. *Spred2*, *Lipt1-Mitd1*, and *Zfp668*) were also identified as such in mouse preimplantation embryos [159]. While all imprinted-like regions had substantial DNA methylation levels in gametes, only some showed gamete specificity, with many displaying similar levels in both oocytes and sperm. Genomic imprinting establishment could thus be occurring in gametes for some imprinted-like loci whereas others may become imprinted during development.

Permanent derepression of MERVL and MT2 LTRs may be linked to gene transcript chimerism

DNA methylation participates in the repression of transposable elements [160]. Loss of DNA methylation can lead to transposable element de-repression, which in turn can influence gene expression regulation [161] and induce genomic instability [162]. LTRs and LINEs being significantly susceptible to permanent CpG hypomethylation during *Dnmt1* inactivation and rescue (Fig. 3B) prompted us to determine whether this was accompanied by increased transcriptional activation, indicative of derepression. Additionally, we sought to explore how their de-repression might impact the regulation of neighboring genes through the generation of chimeric gene transcripts [163].

We initially investigated whether specific LTR and LINE families showed distinct propensities for permanent CpG hypomethylation. The frequency of permanently hypomethylated CpGs within the most abundant LTR families (Fig. 5A)—ERV1 (0.28), ERVK (0.33), ERVL (0.29), and ERVL-MaLR (0.26)—did not substantially deviate from the overall frequency in LTRs (0.31) (Fig. 3A). The frequency in L1 LINEs (0.52) (Supplementary Fig. S5A), the most abundant LINE family, was identical to all LINEs combined (Fig. 3A). Though, when computing the frequencies of permanently hypomethylated CpGs specifically in high-occupancy elements (i.e. genomic occurrences ≥ 500), the vast majority had strikingly higher frequencies (Fig. 5A and Supplementary Fig. S5A). We thus focused on high-occupancy elements to explore if their permanent CpG hypomethylation affected their transcription. Mean CpG methylation levels and total normalized RNA-seq counts of all loci combined were measured for each high-occupancy element across conditions. All high-occupancy L1 elements exhibited permanent mean CpG hypomethylation $\geq 10\%$ (Supplementary Fig. S5B), but none showed major alterations in transcription (total normalized count $\log_2$ fold change > -1 and < 1 in $Dnmt1^{INV}$ and $Dnmt1^{RES}$ versus $Dnmt1^{CTL}$) (Supplementary Fig. S5C). Turning toward high-occupancy LTR elements, MERVL-int and MT2_Mm emerged as the sole elements demonstrating two key characteristics: permanent mean CpG hypomethylation $\geq 10\%$ (Fig. 5B) and notable gradual increase in transcription throughout *Dnmt1* inactivation and rescue, culminating with a $\log_2$ fold change ≥ 1 in $Dnmt1^{RES}$ versus $Dnmt1^{CTL}$ (Fig. 5C). Given the evidence supporting the pivotal roles of MERVL-int and MT2_Mm in zygotic genome activation [164–166] and potency state transitions [167, 168], we undertook a deeper analysis of locus-specific CpG methylation and transcription dynamics. Overall, MERVL-int and MT2_Mm showed highly significant decrease in locus-specific mean CpG methylation levels and increase in locus-specific transcript levels in $Dnmt1^{INV}$ and $Dnmt1^{RES}$ compared to $Dnmt1^{CTL}$ (Fig. 5D–G and Supplementary Table S5). When examining each locus, permanent but gradual increase in transcription occurred at loci exhibiting either temporary or permanent CpG hypomethylation (Fig. 5H–I). Moreover, MERVL-int and MT2_Mm upregulation proximal to gene TSSs (e.g. *Arap2*, *Cwc22*, and *Zfp677*) suggests the generation of associated chimeric gene transcripts (Fig. 5J).

To sum up, high-occupancy LTRs and LINEs exhibited heightened susceptibility to permanent CpG hypomethylation during *Dnmt1* inactivation and rescue. MERVL-int and MT2_Mm LTRs stood out by displaying a progressive increase in transcriptional activation, even at loci where loss of DNA methylation was only temporary. This could reflect a form of epigenetic memory, resulting from changes in chromatin architecture or in the binding of regulatory proteins that persist even after DNA methylation is restored. Additionally, loss of DNA methylation could trigger feedback loops with distal regulatory elements that sustain transcriptional activation, even after the initial trigger is removed. Moreover, in some cases, the resilience of transposable element activation might arise from selective cellular advantages, such as through the generation of chimeric gene transcripts that can forge novel functional outcomes.

Gene expression dysregulation and genomic instability

We next assessed the broader molecular impact of transient DNMT1 loss in mESCs, extending beyond altered epigenomic landscapes. Specifically, we measured changes in gene expression, which can directly result from epigenomic alterations, and examined genomic stability, including the presence of DNA damage and the length of telomeres. DNMT1 contributes to preventing the accumulation of DNA damage by restoring methylation during DNA repair [34], and telomere length control has been linked to DNA methylation regulation [169–171].

We first examined significantly differentially expressed genes (adjusted P-value ≤ 0.05) in $Dnmt1^{INV}$ and $Dnmt1^{RES}$ conditions versus $Dnmt1^{CTL}$, focusing on genes exhibiting dysregulation of considerable magnitude ($\log_2$ fold change ≤ -0.6 or ≥ 0.6). Thousands of genes were

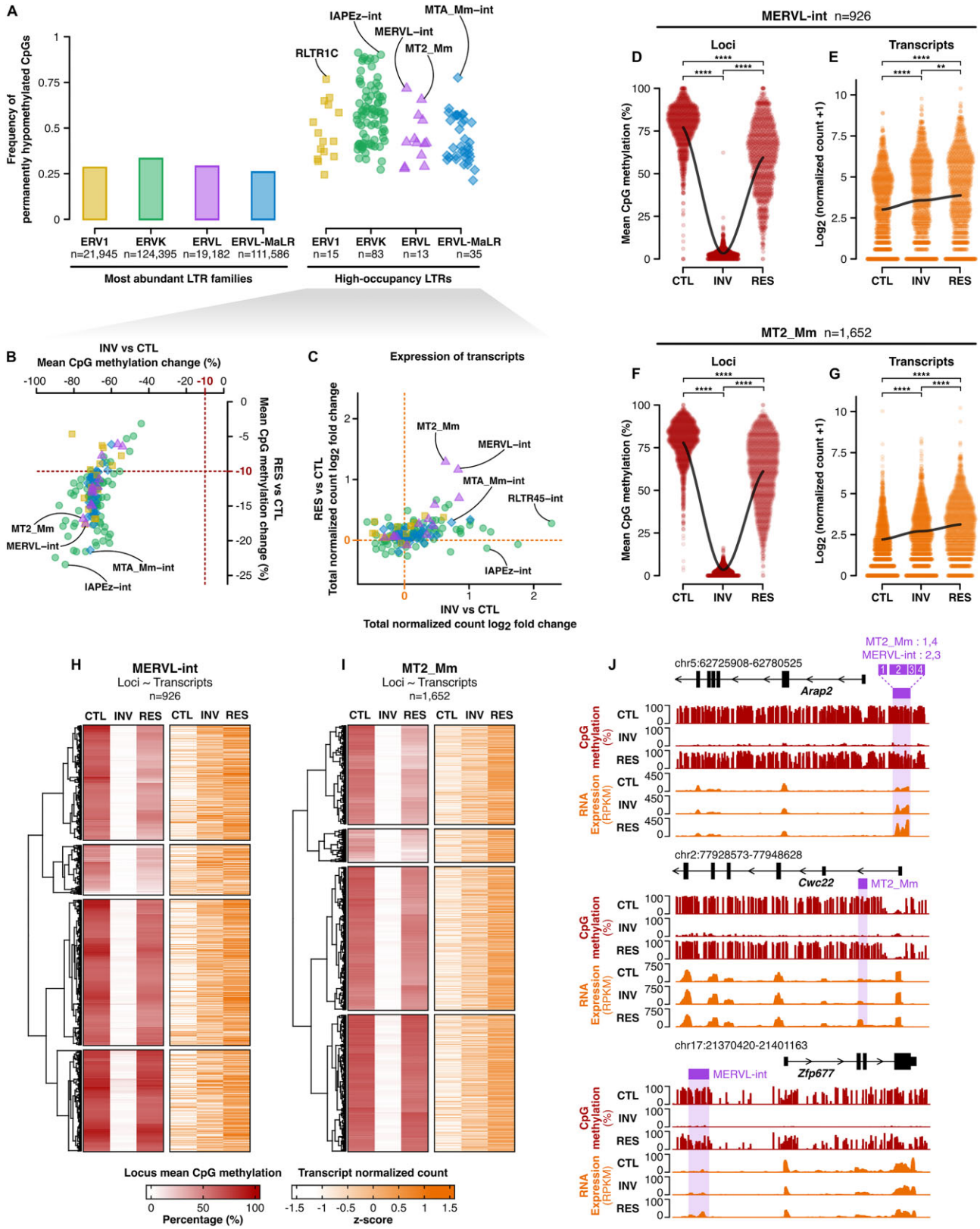

Figure 5. Permanent derepression of MERVL and MT2 LTRs may be linked to gene transcript chimerism. (**A**) Frequency of permanently hypomethylated CpGs in the most abundant LTR families and in high-occupancy LTRs (genomic occurrences ≥ 500). (**B** and **C**) Change in mean CpG methylation levels (EM-seq) and $\log_2$ fold change of total RNA-seq normalized counts, respectively, of high-occupancy LTRs in *Dnmt1*^{INV} and *Dnmt1*^{RES} versus *Dnmt1*^{CTL} (EM-seq: $n = 3$, RNA-seq: $n = 2$ per condition). (**D** and **E**) Pairwise comparisons of MERVL-int locus-specific mean CpG methylation levels and RNA-seq normalized counts in *Dnmt1*^{CTL}, *Dnmt1*^{INV}, and *Dnmt1*^{RES} using the Wilcoxon rank sum test with Benjamini–Hochberg *P*-value adjustment. ** *P*-value ≤ 0.01, **** *P*-value ≤ 0.0001. (**F** and **G**) Pairwise comparisons of MT2-Mm locus-specific mean CpG methylation levels and RNA-seq normalized counts in *Dnmt1*^{CTL}, *Dnmt1*^{INV}, and *Dnmt1*^{RES} using the Wilcoxon rank sum test with Benjamini–Hochberg *P*-value adjustment. (**H** and **I**) *Z*-score normalization of locus-specific CpG methylation level and RNA-seq normalized count for MERVL-int and MT2_Mm. (**J**) Genomic signal tracks showing CpG methylation and RNA expression for MERVL-int and MT2-Mm loci proximal to TSSs. See also Supplementary Table S5.

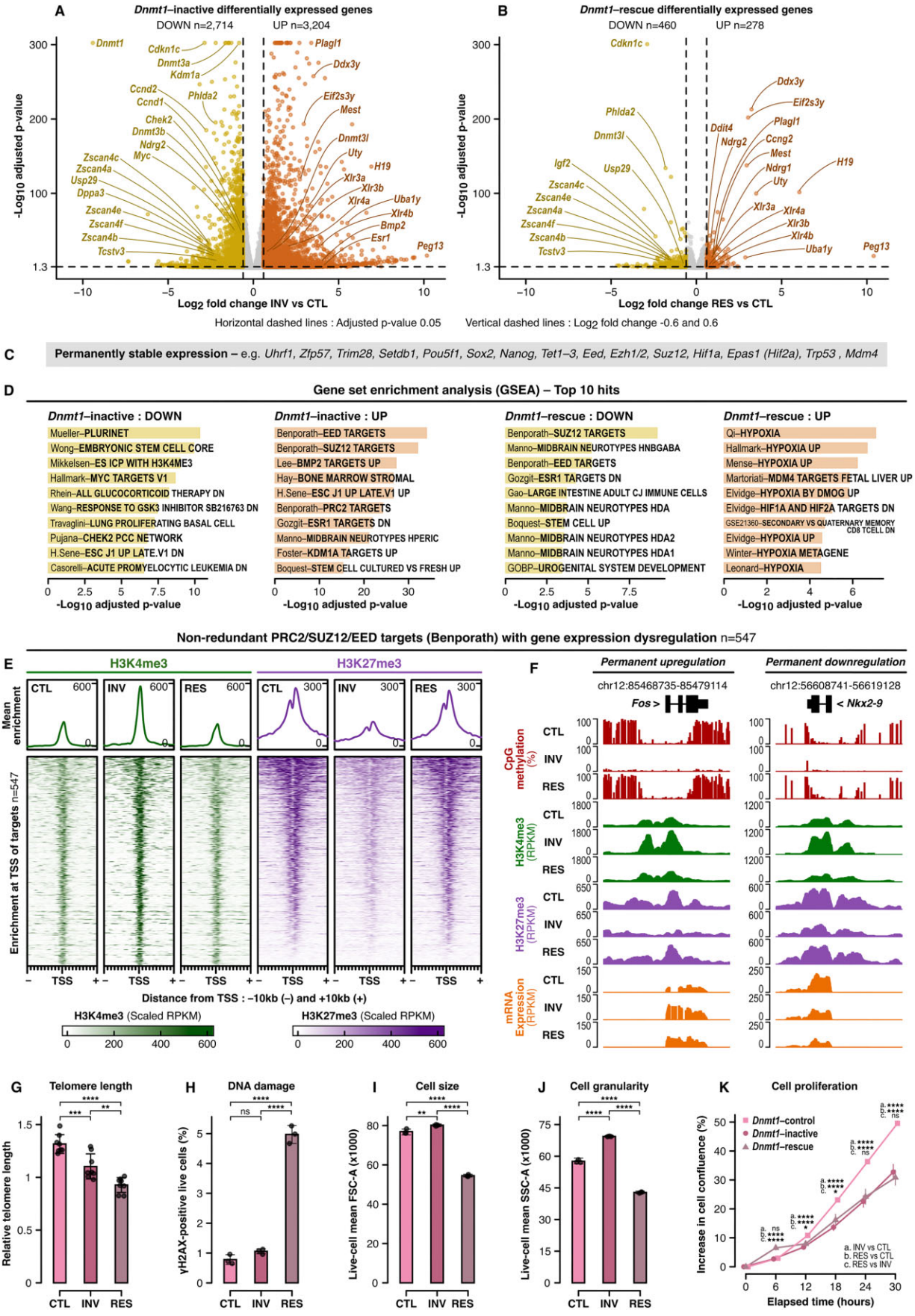

Figure 6. Gene expression dysregulation, genomic instability, and altered cellular processes. (**A** and **B**) Differentially expressed genes in *Dnmt1*^{INV} and *Dnmt1*^{RES} versus *Dnmt1*^{CTL} determined by an adjusted *P*-value ≤ 0.05 and $\log_2$ fold change ≤ −0.6 or ≥ 0.6 using mRNA sequencing ($n = 3$ per

dysregulated in $Dnmt1^{INV}$ (downregulated: $n = 2714$; upregulated; $n = 3204$) (Fig. 6A and Supplementary Table S6), whereas in $Dnmt1^{RES}$, the number was notably reduced but still in the hundreds (downregulated: $n = 460$; upregulated; $n = 278$) (Fig. 6B and Supplementary Table S6). To reveal patterns of gene expression dysregulation, we categorized genes based on their downregulation, upregulation, or stable expression in $Dnmt1^{INV}$ and $Dnmt1^{RES}$ (Fig. 6C and Supplementary Fig. S6A). Interestingly, *Dnmt3a* and *Dnmt3b* exhibited temporary downregulation, whereas *Dnmt3l* demonstrated dynamic up- and downregulation. Conversely, other key players in DNA methylation such as *Uhrf1*, *Tet1-3*, *Zfp57*, and *Trim28*, maintained stable expression. *Kdm1a*, known for gene repression via H3K4 demethylation, was notably temporarily downregulated, possibly contributing to the marked H3K4me3 increase in $Dnmt1^{INV}$ (Fig. 2A). Dysregulation extended to cell cycle regulators, with *Myc*, *Ccnd1-2*, and *Chek2* exhibiting temporary downregulation, and *Ccng2* showing latent upregulation. Additionally, cellular stress and DNA damage response genes were affected, with *Ndrg1* and *Ddit4* showing latent upregulation, and *Ndrg1* showing dynamic down- and upregulation. Potency state regulators were also dysregulated, including temporary downregulation of *Dppa3* and permanent downregulation of *Zscan4a-f* and *Tcstv3*, with *Zscan4a-f* and *Tcstv3* being specifically recognized for their role in telomere elongation [172, 173]. Notably, an increase and spreading of repressive H3K9me3 across the promoters and gene bodies of *Zscan4a* and *Zscan4d* was evident in $Dnmt1^{INV}$ and $Dnmt1^{RES}$ (Supplementary Fig. S6B). Moreover, permanent upregulation of *Xlr3a-b* and *Xlr4a-b*, part of an X-linked cluster known for tissue-specific imprinted gene expression in mice [174], and of *Uba1y*, *Eif2s3y*, *Uty*, and *Ddx3y* within a Y-linked cluster were of particular interest given the significant susceptibility of sex chromosomes to permanent CpG hypomethylation (Fig. 3B). In fact, promoters of *Xlr3a*, *Xlr4a*, *Eif2s3y*, and *Uty* showed permanent CpG hypomethylation and increase of permissive H3K4me3 and H3K27ac in $Dnmt1^{INV}$ and $Dnmt1^{RES}$ (Supplementary Fig. S6C). Despite extensive and dynamic changes in gene expression, key pluripotency markers (*Pou5f1*, *Sox2*, and *Nanog*) remained stably expressed during *Dnmt1* inactivation and rescue (Fig. 6C), suggesting that mESC pluripotency and differentiation potential were generally preserved.

We then proceeded with GSEA of down- and upregulated genes in $Dnmt1^{INV}$ and $Dnmt1^{RES}$, selecting their top 10 significantly enriched gene sets (Fig. 6D). EED [175], SUZ12 [175], PRC2 [175], and KDM1A [176] targets stood out among upregulated gene sets in $Dnmt1^{INV}$, and, interestingly, EED and SUZ12 targets were conversely enriched in $Dnmt1^{RES}$ downregulated genes. PRC2, comprising SUZ12 and EED among its components, mediates the deposition of H3K27me3 in bivalent developmental gene promoters [177]. Nearly all promoters of dysregulated PRC2/SUZ12/EED target genes [175] (nonredundant: $n = 547$) exhibited a simultaneous sharp surge in H3K4me3 and decline in H3K27me3 centered at their TSS in $Dnmt1^{INV}$, with levels returning to baseline in $Dnmt1^{RES}$ (Fig. 6E). This temporary transition to an active chromatin state occurred independently of changes in CpG methylation levels within TSS regions, which remained consistently very low across all conditions (median levels < 5.5%), and independently of gene expression dysregulation patterns (Supplementary Fig. S6D and Supplementary Table S7), as exemplified by epigenetic profiles of *Fos* and *Nkx2-9* (Fig. 6F). Additional compelling insights emerged from our GSEA analysis. Pluripotency network [178], ESC core [179], MYC targets [136], and CHEK2 network [180] gene sets were enriched among $Dnmt1^{INV}$ downregulated genes, while $Dnmt1^{RES}$ upregulated genes showed predominant enrichment in hypoxia gene sets [136, 181–185], suggesting disturbances cell cycle regulation and an increase in cellular stress. In fact, throughout *Dnmt1* inactivation and rescue, we detected signs of genomic instability, indicative of cellular stress. We observed a progressive shortening of telomere length (Fig. 6G) and a latent increase in γH2AX (Fig. 6H), a marker for DNA double-strand breaks.

In summary, while *Dnmt1* rescue restored the expression of most genes that had been dysregulated following its inactivation, not all expression levels returned to baseline, with the rescue also resulting in additional gene expression dysregulation. Dysregulation of cell cycle regulators, downregulation of telomere elongation factors, and upregulation of cellular stress and DNA damage response genes were notably detected, corresponding with *Dnmt1* inactivation and rescue leading to shortened telomeres and increased DNA damage. These results highlight the far-reaching molecular consequences of lacking continuous DNA methylation maintenance, extending beyond altered epigenomic landscapes by disrupting gene expression levels and inducing genomic instability.

Morphological and functional cellular responses

ESCs are characterized by their high cellular plasticity, which grants them resilience to significant epigenetic perturbations [36, 76–78]. Still, we questioned whether the molecular alterations caused by transient *Dnmt1* inactivation would manifest in cellular responses. To address this, we assessed mESC morphology (size and internal complexity) and functional proper-

←

condition) analyzed with the DESeq2 software. (**C**) Notable genes with stable expression in $Dnmt1^{INV}$ and $Dnmt1^{RES}$ versus $Dnmt1^{CTL}$. (**D**) GSEA for down- and upregulated genes in $Dnmt1^{INV}$ and $Dnmt1^{RES}$. (**E**) Signal enrichment of H3K4me3 and H3K27me3 in $Dnmt1^{CTL}$, $Dnmt1^{INV}$, and $Dnmt1^{RES}$ at TSSs of PRC2/SUZ12/EED nonredundant targets exhibiting gene expression dysregulation in $Dnmt1^{INV}$ and/or $Dnmt1^{RES}$ identified in panel (D). RPKM values were scaled between 0 and 0.99 quantiles to mitigate the presence of outliers. (**F**) Genomic signal tracks showing CpG methylation, H3K4me3, H3K27me3, and mRNA expression for PRC2/SUZ12/EED targets *Fos* and *Nkx2-9* in $Dnmt1^{CTL}$, $Dnmt1^{INV}$, and $Dnmt1^{RES}$. (**G**) Pairwise comparisons of relative telomere length in $Dnmt1^{CTL}$, $Dnmt1^{INV}$, and $Dnmt1^{RES}$ measured by qPCR and the delta-delta C_t method, with normalization to reference single-copy gene *Rplp0* and relativization to reference DNA from R1 mESCs ($n = 8$ per condition). (**H–J**) Pairwise comparisons of the percentage of γH2AX-positive live cells (DNA damage), live-cell mean forward scatter area (FSC-A; cell size), live-cell mean side scatter area (SSC-A; cell granularity i.e. internal complexity), respectively, in $Dnmt1^{CTL}$, $Dnmt1^{INV}$, and $Dnmt1^{RES}$ measured by FACS ($n = 3$ per condition). (**K**) Pairwise comparisons of cell proliferation rate for $Dnmt1^{CTL}$, $Dnmt1^{INV}$, and $Dnmt1^{RES}$ measured by the increase in confluency over 30 h ($n = 3$ per condition). All pairwise comparisons were conducted using one-way ANOVA with Tukey's HSD test with *P*-value adjustment. ns *P*-value > 0.05, * *P*-value ≤ 0.05, ** *P*-value ≤ 0.01, *** *P*-value ≤ 0.001, **** *P*-value ≤ 0.0001. See also Supplementary Tables S6 and S7 and Supplementary Fig. S6 and S7.

ties, including proliferation rate and differentiation potential toward germ layer cell types (endoderm, mesoderm, and ectoderm). The impact on gene expression patterns in germ layer cells was also examined.

Dynamic changes in cell size and internal complexity (i.e. granularity) were observed throughout *Dnmt1* inactivation and rescue in mESCs, increasing in $Dnmt1^{INV}$ and decreasing in $Dnmt1^{RES}$ (Fig. 6I and J, and Supplementary Fig. S7A), and cell proliferation rate (Fig. 6K) was reduced in both $Dnmt1^{INV}$ and $Dnmt1^{RES}$. These results reflect altered cell cycle dynamics, consistent with DNMT1's critical role during cell division [29–32]. The molecular and cellular alterations in mESCs prompted us to investigate if temporary inactivation of *Dnmt1* would have a lasting impact on their differentiation. To verify this, $Dnmt1^{CTL}$ and $Dnmt1^{RES}$ mESCs were differentiated into endoderm, mesoderm, and ectoderm monolayers (Fig. 7A) which were sorted based on lineage-specific cell surface markers. Similar percentages of marker-positive cells were obtained in $Dnmt1^{CTL}$ and $Dnmt1^{RES}$ derived germ layer lineages (Supplementary Fig. S7B), and principal component analysis of gene expression showed comparable separation of mESCs and differentiated cells for both $Dnmt1^{CTL}$ and $Dnmt1^{RES}$ conditions (Supplementary Fig. S7C). $Dnmt1^{CTL}$ and $Dnmt1^{RES}$ ectoderm inductions were similarly successful; compared to mESCs, pluripotency markers were all markedly lower, and differentiation markers were all markedly higher, whereas some, mostly minor, differences in marker levels between $Dnmt1^{CTL}$ and $Dnmt1^{RES}$ inductions were noticeable for endoderm and mesoderm (Supplementary Fig. S7D–F). Overall, transient inactivation of *Dnmt1* therefore did not appear to have a major impact on the differentiation potential of mESCs. However, differential gene expression analysis in $Dnmt1^{RES}$ versus $Dnmt1^{CTL}$ derived germ layers revealed hundreds of dysregulated genes (Fig. 7B and Supplementary Table S6), compellingly showing enrichment for PRC2 [175], SUZ12 [175], and EED [175] targets (Fig. 7C) as was observed in mESCs (Fig. 6D). Among $Dnmt1^{RES}$ cell types, endoderm had the highest number of dysregulated genes, followed by mESCs, mesoderm, and ectoderm (Fig. 7D). Down- and upregulated genes in $Dnmt1^{RES}$ cell types were primarily cell type-specific, though some were shared among multiple $Dnmt1^{RES}$ cell types such as *Dnmt3l* downregulated in mESCs, endoderm and mesoderm, and *Sall3* upregulated in all germ layers (Fig. 7E and F).

Taken together, these findings demonstrate that despite their high cellular plasticity, mESCs exhibited morphological and functional responses to transient loss of DNMT1 activity, including reduced cell size, internal complexity and proliferation rate as well as altered gene expression profiles upon their differentiation toward germ layers. Dysregulation of gene expression in germ layers was mostly lineage-specific, illustrating how the impact of epigenetic perturbations can be cell type-specific, thus resulting in phenotypic variation depending on the affected cells [20–22]. However, stemness properties remained well-preserved following *Dnmt1* inactivation and rescue in mESCs: pluripotency marker genes were stably expressed, mESCs retained the ability to proliferate indefinitely, albeit at a slower rate, and the potential of mESCs for differentiation toward germ layers was generally conserved.

Delaying *Dnmt1* rescue until after differentiation initiation worsens molecular and cellular outcomes

We demonstrated that rescuing DNMT1 activity was insufficient to fully counteract the effects of its loss in mESCs, inducing permanent and post-rescue molecular and cellular responses as well as lasting effects upon differentiation toward ectoderm, mesoderm, and endoderm germ layers. Next, we hypothesized that delaying *Dnmt1* rescue after differentiation initiation would lead to worse outcomes, as differentiated cells are typically less resilient to epigenetic disturbances due to cellular plasticity decreasing during differentiation [186, 187]. We tested this hypothesis using embryoid bodies which are 3D spheroid aggregates of ESCs that spontaneously differentiate into early developmental cell types, enabling longitudinal studies of certain aspects of developmental processes [188, 189].

Embryoid bodies were derived from *Dnmt1*-control mESCs, *Dnmt1*-rescue mESCs, as well as from *Dnmt1*-inactive mESCs for which *Dnmt1* inactivation was maintained throughout the 10 days of embryoid body formation. On day 5, *Dnmt1* was reactivated in a subset of *Dnmt1*-inactive embryoid bodies for post-differentiation rescue of *Dnmt1*. Four experimental conditions were thus included during embryoid body formation: *Dnmt1*-control, *Dnmt1*-inactive, *Dnmt1*-rescue, and post-differentiation *Dnmt1*-rescue (Fig. 8A). Successful inactivation and post-differentiation rescue of *Dnmt1* in embryoid bodies were confirmed by western blot (Supplementary Fig. S8A). Throughout embryoid body formation, morphological and molecular analyses were conducted. Daily bright-field microscopy images were taken of embryoid bodies for measuring their size and circularity, and mRNA sequencing was performed on days 5 and 10.

On day 2 of embryoid body formation, *Dnmt1*-rescue embryoid bodies were slightly smaller than *Dnmt1*-control embryoid bodies but rapidly caught up in size, whereas *Dnmt1*-inactive embryoid bodies remained substantially smaller throughout all 10 days of embryoid body formation (Fig. 8B and C, and Supplementary Fig. S8B). Rescuing *Dnmt1* on day 5 in *Dnmt1*-inactive embryoid bodies triggered a marked, progressive increase in growth; by day 10, post-differentiation *Dnmt1*-rescue embryoid bodies were substantially larger than *Dnmt1*-inactive embryoid bodies, though still smaller than both *Dnmt1*-control and *Dnmt1*-rescue embryoid bodies (Fig. 8B and C, Supplementary Fig. S8B). However, post-differentiation rescue of *Dnmt1* could not prevent the eventual loss of embryoid body circularity resulting from *Dnmt1* inactivation during early embryoid body formation. Despite being reasonably circular up to day 5, *Dnmt1*-inactive and post-differentiation *Dnmt1*-rescue embryoid bodies progressively developed highly irregular shapes, while *Dnmt1*-control and *Dnmt1*-rescue embryoid bodies consistently maintained nearly perfect circularity (Fig. 8B and D, and Supplementary Fig. S8C).

We then performed gene expression analysis on days 5 and 10 of embryoid body formation, revealing extensive alterations in *Dnmt1*-inactive embryoid bodies that worsened over time. Principal component analysis showed that their gene expression profiles progressively diverged from controls between days 5 and 10 (Fig. 8E), with the number of differentially expressed genes increasing from 3725 on day 5 to 5469 on day 10 (Fig. 8F). Post-differentiation *Dnmt1*-rescue

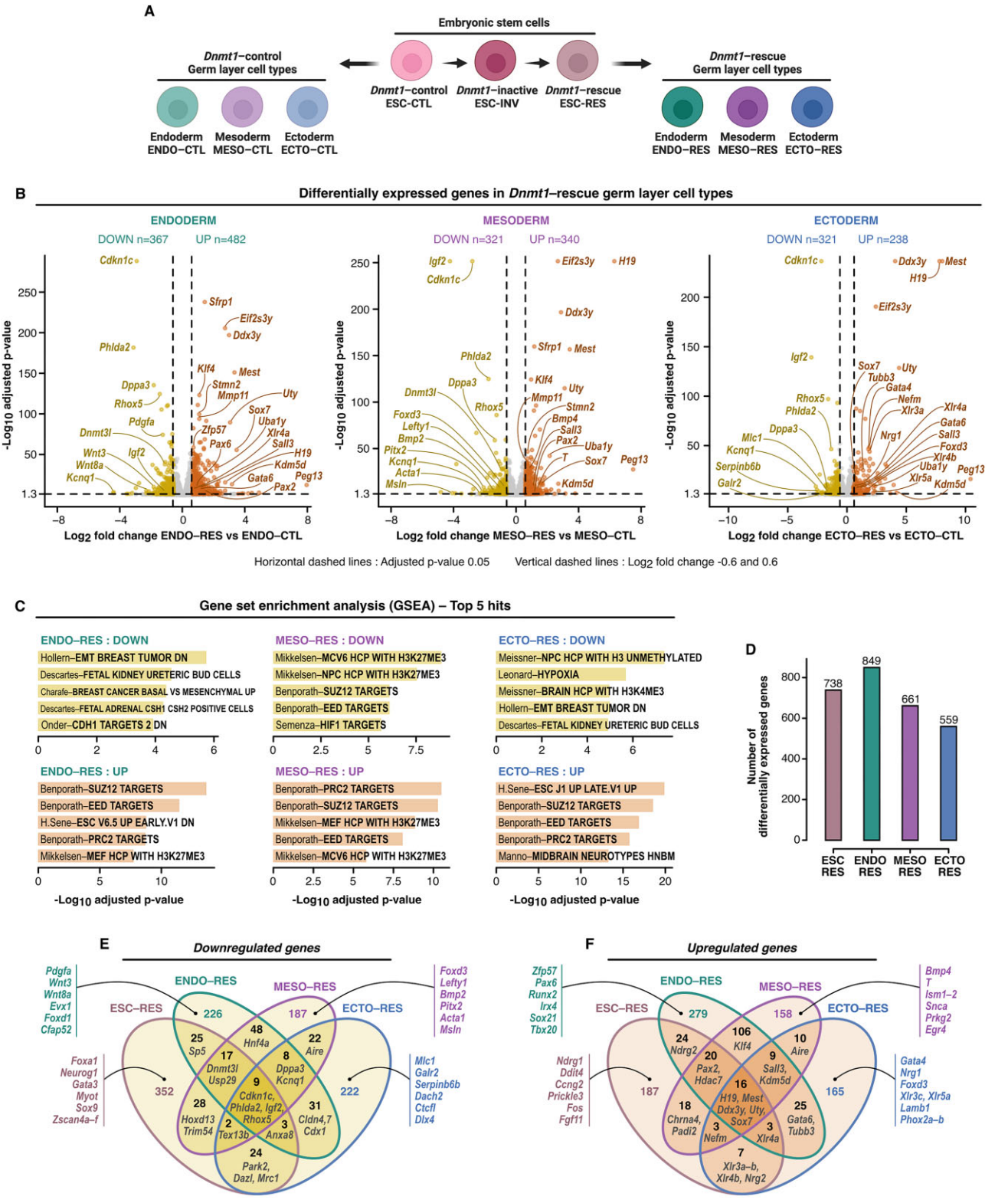

Figure 7. Lasting effects on gene expression patterns upon differentiation to embryonic germ layers. (**A**) Schematic diagram depicting *Dnmt1*^{CTL} and *Dnmt1*^{RES} differentiation into germ layer monolayers ($n = 3$ per differentiation). Created in BioRender: Dupas, T. (2025) https://BioRender.com/y05v644. (**B**) Differential gene expression in *Dnmt1*^{RES} versus *Dnmt1*^{CTL} endoderm, mesoderm and ectoderm determined by an adjusted *P*-value ≤ 0.05 and $\log_2$ fold change ≤ -0.6 or ≥ 0.6 using mRNA sequencing ($n = 3$ per differentiation) analyzed with the DESeq2 software. (**C**) GSEA for down- and upregulated genes in *Dnmt1*^{RES} germ layers. (**D**) Total number of differentially expressed genes in *Dnmt1*^{RES} cell types. (**E** and **F**) Overlap of downregulated and upregulated genes among *Dnmt1*^{RES} cell types. See also Supplementary Table S6 and Supplementary Fig. S7.

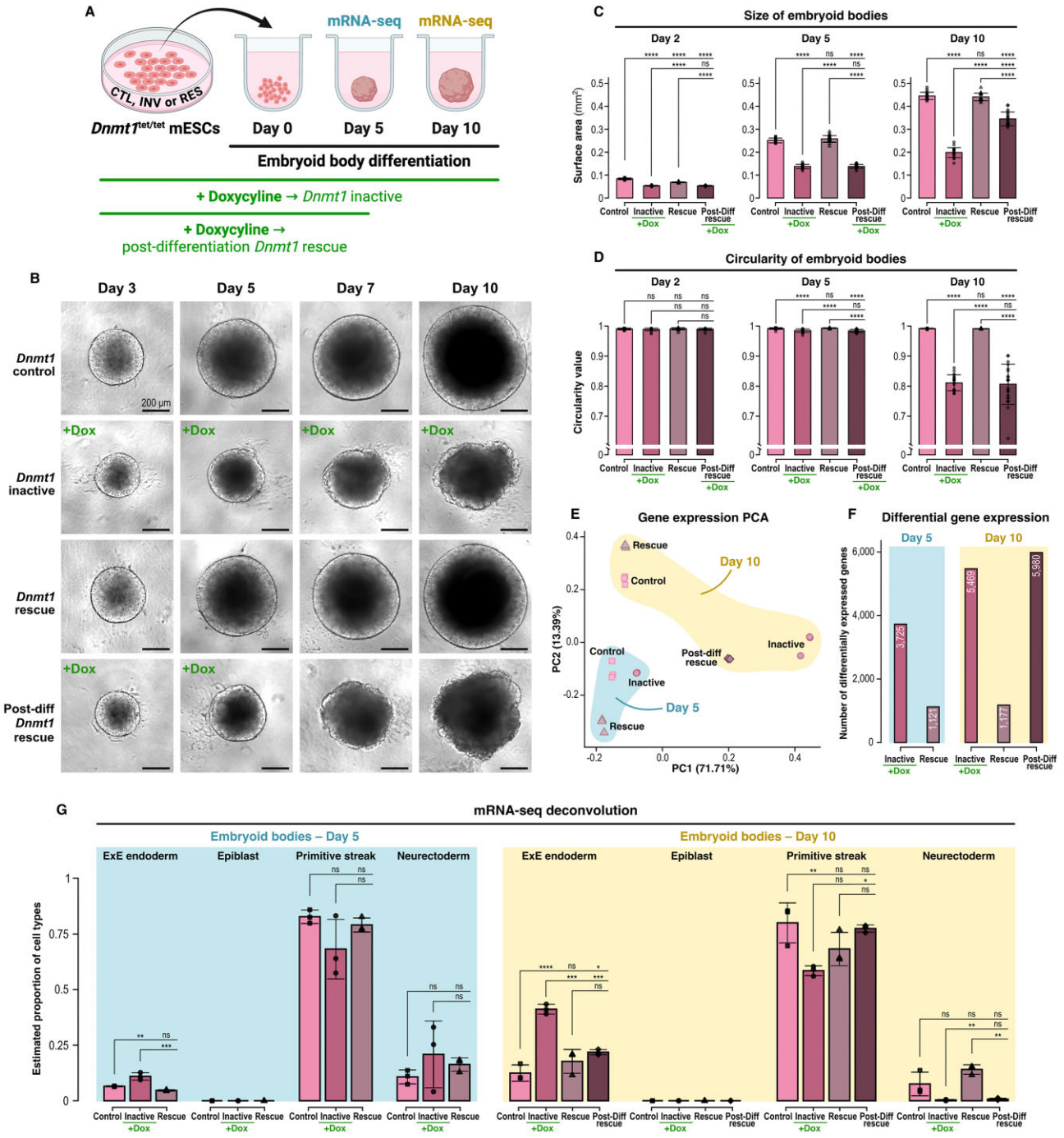

Figure 8. Delaying *Dnmt1* rescue until after differentiation initiation worsens molecular and cellular outcomes. (**A**) Schematic diagram depicting embryoid body formation including four experimental conditions: *Dnmt1*-control, *Dnmt1*-inactive, *Dnmt1*-rescue, and post-differentiation *Dnmt1*-rescue. Embryoid bodies ($n = 192$ per condition) were derived from the same *Dnmt1*$^{tet/tet}$ mESC culture. Created in BioRender: Dupas, T. (2025) https://BioRender.com/f72a244. (**B**) Bright-field microscopy images of one embryoid body per condition taken on days 3, 5, 7, and 10. (**C**) Size and (**D**) circularity of embryoid bodies on days 2, 5, and 10 determined by measuring their surface area and perimeter on bright-field microscopy images using the ImageJ software. Daily images were taken of the same 20 embryoid bodies per condition. Surface area was used as an indicator of size and circularity was calculated with the formula $4\pi \times \text{Area}/\text{Perimeter}^2$. (**E**) Principal component analysis of gene expression measured on day 5 and day 10 by mRNA sequencing ($n = 3$ per condition with pooled embryoid bodies). A greater divergence in gene expression profiles is represented by the distance between samples along the *x*-axis (PC1), compared to the *y*-axis (PC2). (**F**) Number of differentially expressed genes in *Dnmt1*-inactive, *Dnmt1*-rescue, and post-differentiation *Dnmt1*-rescue embryoid bodies versus *Dnmt1*-control embryoid bodies on day 5 and day 10 determined by an adjusted *P*-value ≤ 0.05 and log2 fold change ≤ -0.6 or ≥ 0.6 using mRNA sequencing analyzed with the DESeq2 software. (**G**) Estimated proportion of ExE endoderm, epiblast (pluripotent), primitive streak (mesendoderm), and neurectoderm cell types in embryoid bodies on days 5 and 10 determined by deconvoluting raw counts using single-cell data from mouse gastrulation embryos (embryonic day 7.75). All pairwise comparisons were conducted using one-way ANOVA with Tukey's HSD test and *P*-value adjustment. ns *P*-value > 0.05, * *P*-value ≤ 0.05, ** *P*-value ≤ 0.01, *** *P*-value ≤ 0.001, **** *P*-value ≤ 0.0001. See also Supplementary Fig. S8.

embryoid bodies exhibited a higher number of significantly dysregulated genes than *Dnmt1*-inactive embryoid bodies on day 10 (Fig. 8F), but their overall gene expression profiles were more aligned with controls (Fig. 8E). Although *Dnmt1*-rescue embryoid bodies displayed similar growth and morphology compared to controls, gene expression was substantially affected, albeit to a lesser extent than in the *Dnmt1*-inactive and post-differentiation *Dnmt1*-rescue conditions (Fig. 8E and F). Principal component analysis revealed distinct separation between the gene expression profiles of *Dnmt1*-rescue and *Dnmt1*-control embryoid bodies on days 5 and 10 of their formation (Fig. 8E), with over 1100 significantly differentially expressed genes identified at each time point (Fig. 8F). Notably, the number of differentially expressed genes was considerably higher in embryoid bodies than in monolayer germ layers derived from *Dnmt1*-rescue mESCs (Fig. 7D), likely due to reduced cellular plasticity in 3D versus monolayer cell cultures [190]. Monolayer cell cultures often exhibit greater cellular plasticity than 3D cultures because they lack the spatial and mechanical constraints present in a 3D environment, allowing cells to more freely adapt their shape, interactions, and gene expression. Conversely, 3D cultures mimic *in vivo* conditions more closely, promoting cell polarity, differentiation, and tissue-specific behaviors that restrict plasticity.

Next, we deconvoluted gene expression profiles [147, 148] using single-cell RNA-seq data from mouse gastrulation embryos [146] to estimate the proportions of inner cell mass-derived early developmental cell types within embryoid bodies across experimental conditions and time points (Fig. 8G). Specifically, we assessed the proportion of extraembryonic (ExE) endoderm cells, epiblast cells (pluripotent precursors to embryonic germ layers), primitive streak cells (precursors to mesoderm and endoderm lineages), and neurectoderm cells (precursors to neural tissues). As expected, embryoid bodies across all experimental conditions showed no proportion of epiblast cells on days 5 and 10. Cell type proportions in *Dnmt1*-rescue embryoid bodies were similar to those in controls at both time points, while *Dnmt1*-inactive and post-differentiation *Dnmt1*-rescue embryoid bodies exhibited significant differences. Most notable was the higher proportion of ExE endoderm cells in *Dnmt1*-inactive embryoid bodies that continued to increase over time, with post-differentiation rescue of *Dnmt1* partially preventing this cell type proportion shift toward ExE endoderm cells. This observation aligns with findings from a previous study showing that DNA methylation is essential for the differentiation of embryonic lineages but dispensable for ExE lineages; triple DNMT knockout mESCs exhibited progressive cell death during their differentiation into epiblast-derived cells but maintained viability when differentiating into ExE cells, both *in vitro* and *in vivo* [191].

Overall, *Dnmt1* inactivation in mESCs and throughout embryoid body formation caused severely stunted growth, abnormal morphology, and gene expression alterations accompanied by a substantial increase in the estimated proportion of ExE endoderm cells. Rescuing *Dnmt1* midway through embryoid body formation partially restored growth and estimated cell type proportions and mitigated the severity of gene expression alterations but failed to prevent severe morphological abnormalities. In contrast, rescuing *Dnmt1* in mESCs prior to embryoid body formation supported growth, morphology, and estimated cell type proportions comparable to the controls and led to more moderate differences in gene expression. These findings illustrate the escalating impact of an epigenetic perturbation as cellular plasticity decreases and demonstrate the disadvantages of a delayed epigenetic rescue intervention, underscoring the importance of early intervention for better developmental outcomes.

Discussion

In this study, *Dnmt1* inactivation and rescue in mESCs had a wide-ranging molecular impact, leading to DNA methylation and histone modification alterations, gene expression dysregulation, genomic instability, and transposable element derepression. Transient *Dnmt1* inactivation also induced morphological and functional responses in mESCs and had lasting effects upon their differentiation, with post-differentiation rescue of *Dnmt1* worsening outcomes. Moreover, transient *Dnmt1* inactivation in mESCs enabled the discovery of 20 regions with imprinted-like signatures.

Genomic imprinting mechanisms and discovery of novel imprinted regions

mESC and embryo models remain invaluable tools for deciphering genomic imprinting mechanisms and uncovering novel imprinted regions through disruption of genomic imprinting maintenance machinery [36, 37, 139, 159]. However, characterization of imprinted regions is highly complex due to diverse regulatory factors and epigenetic modifications, often defying a robust universal mechanistic paradigm.

While DNA methylation and H3K9me3 are extensively investigated in genomic imprinting, cellular and animal mouse studies have implicated additional histone modifications. Imprinted (i.e. repressed) alleles, comarked by DNA methylation and H3K9me3 [84, 107, 159, 192], may occasionally also display H3K27me3 [84, 192], whereas H3K4me2/3 [84, 192, 193] and H3K27ac [194] characterize permissive alleles, which can exhibit bivalency with concurrent H3K27me3 [84, 192, 193]. This study was distinctive for simultaneously profiling H3K4me3, H3K4me1, H3K27ac, and H3K27me3, alongside customary DNA methylation and H3K9me3, offering an unprecedented perspective on the complex and divergent nature of imprinting mechanisms. While derepression of imprinted regions following *Dnmt1* inactivation, marked by DNA hypomethylation and decreased H3K9me3, was consistently accompanied by increases in H3K4me3 and H3K4me1, fluctuations in H3K27ac and H3K27me3 varied across different imprinted regions, illustrating the divergent nature of imprinting mechanisms. In certain instances, increased H3K4me3 overlapped with increased H3K4me1, and increased H3K27ac overlapped with H3K27me3—an intriguing observation given that these modification pairs are mutually exclusive as they occur on the same amino acid residue. This could suggest that imprinted regions can harbor asymmetrical nucleosome modifications [195] or exhibit cellular heterogeneity in their epigenetic profiles. Additionally, these pairs of mutually exclusive histone modifications might reside on different alleles. Derepression of the imprinted allele could induce epigenetic alterations on the opposing allele through transvection effects, a form of epigenetic crosstalk between alleles [196–199]. Further investigation of these potential mechanisms would benefit from the use of mESCs with parental single-nucleotide polymorphisms, enabling allele-specific profiling of epigenetic marks and chro-

matin interactions. Moreover, the role of H3K4me1 in genomic imprinting has remained unexplored until now, but its correlation with enhancer activity [200–203] imputes relevance for permissiveness of imprinted loci, a notion supported by the increased H3K4me1 at derepressed imprinted regions detected this study. H3K4me1 can help distinguish promoter versus enhancer activity, and active versus poised states, valuable nuances for elucidating how imprinted regions regulate gene expression.

Epigenetic analysis of imprinted regions during *Dnmt1* inactivation and rescue in mESCs uncovered potential novel imprinted regions. These imprinted-like regions exhibited remarkably similar epigenetic responses to transient *Dnmt1* inactivation as those observed in known imprinted regions. Notably, three of the imprinted-like regions identified in this study—*Spred2*, *Lipt1-Mitd1*, and *Zfp668*—have also been characterized as imprinted-like in mouse preimplantation embryos [159]. Imprinted regions play a crucial role in development by regulating the expression of genes that are predominantly essential for developmental processes [154–156]. In humans, *LIPT1* is the causative gene for lipoyltransferase 1 deficiency, a rare inborn metabolism disorder with which *MITD1* is also associated [204–207], and *SPRED2* is a causative gene for Noonan syndrome 14 [208], a severe developmental disorder. Additional imprinted-like regions discovered in this study may also be linked to genes involved in human diseases, such as *REPIN1* linked to nonalcoholic fatty liver disease [209] and polycystic ovary syndrome [210], *HCN2* to epilepsy [211–214], *RNF216* to cerebellar ataxia–hypogonadism syndrome [215, 216], and *VSIG10* to COVID-19 [217]. In this study, these genes became dysregulated upon *Dnmt1* inactivation, when imprinted-like regions were derepressed, suggesting that their regulation may possibly be influenced by their associated imprinted-like region. Therefore, future work exploring the developmental importance of these imprinted-like regions could help unveil novel associations with human diseases.

Wide-ranging molecular and cellular influence of DNMT1

Beyond genomic imprinting maintenance, DNMT1 maintains global DNA methylation profiles [29–32] and contributes to preserving genomic stability [34] during cell division. Through noncatalytic mechanisms [55–58], it can also influence broader epigenomic networks [59, 60], including chromatin conformation, histone modifications, and gene expression.

In the S phase of the cell cycle, DNMT1 methylates newly synthesized DNA [29–32] through its interaction with proliferating cell nuclear antigen (PCNA) [218, 219] and restores methylation following DNA repair [34]. Stressful conditions such as viral infection [220], inflammation [221], or DNA hypomethylation due to DNMT1 depletion [222] can induce cell cycle arrest in G1, preventing DNA damage accumulation in S phase. Progression to S phase despite stress can increase DNA damage, triggering the G2/M checkpoint for G2 arrest [223, 224]. In this study, *Dnmt1* inactivation in mESCs led to downregulation of *Ccnd1/2*, essential for G1/S transition [225–228], whereas *Ccng2*, implicated in G1 and G2 arrest [229–232], was upregulated after *Dnmt1* rescue alongside increased DNA damage. Permanent reduction of mESC proliferation rate throughout inactivation and rescue of *Dnmt1* could therefore be linked to increased cell cycle arrest, in G1 for $Dnmt1^{INV}$ due to drastic DNA methylation and histone modification alterations and in either G1 or G2 for $Dnmt1^{RES}$. Less severe epigenomic changes in $Dnmt1^{RES}$ could have allowed some cells to escape G1 arrest, culminating in DNA damage accumulation and G2/M checkpoint activation. Another potential trigger of cell cycle arrest in $Dnmt1^{INV}$ and $Dnmt1^{RES}$ was telomere shortening [233–235], which may have occurred due to permanent downregulation of *Zscan4a-f* [172] and *Tcstv3* [173], required for telomere elongation in mESCs.

Moreover, *Zscan4a-f* and *Tcstv3* are part of a mouse 2-cell embryo (2C) gene network activated in rare mESC subpopulations as they cycle in and out of a 2C-like totipotent state [167, 168]. This 2C-like totipotent state is further characterized by decreased global DNA methylation levels, absence of pluripotency marker OCT4/POU5F1, derepression of MERVL and MT2 LTRs, and generation of MERVL- and MT2-derived chimeric gene transcripts [167, 168]. This study showed that *Dnmt1* inactivation and rescue in mESCs led to permanent reduction of global DNA methylation and permanently derepressed MERVL and MT2 LTRs with evidence of associated gene transcript chimerism but did not affect *Oct4/Pou5f1* expression levels. This could indicate atypical potency state transitions in $Dnmt1^{RES}$ mESCs, potentially compromising their proliferation rate and other cellular properties, such as their morphological features. In fact, $Dnmt1^{RES}$ mESCs exhibited reduced cell size and internal complexity. Conversely, Eckersley-Maslin *et al.* did not observe MERVL upregulation upon *Dnmt1* repression in mESCs [168]. However, they repressed *Dnmt1* for only three days, after which mean whole-genome and MERVL-specific DNA methylation were both reduced to ∼30%, in contrast to six days of *Dnmt1* repression in this study, where mean levels were reduced to ∼3.5% and ∼3.2%, respectively. Absence of DNMT1 for just three days was likely insufficient to trigger the same magnitude of effects observed in this study, where DNMT1 was absent for twice as long, highlighting how the duration of an epigenetic perturbation significantly influences the severity of the resulting outcomes.

The impact of transient *Dnmt1* inactivation on cellular functions was further evidenced by altered gene expression profiles in germ layers derived from $Dnmt1^{RES}$ mESCs. Lineage-specific and pan-lineage gene expression alterations were observed, with endoderm and mesoderm being more severely affected than ectoderm. Downregulation of *Dnmt3l* in $Dnmt1^{RES}$ mESCs persisting only in endoderm and mesoderm could have instigated deviations in their differentiation trajectories, as DNMT3L is a crucial co-factor for DNMT3A-mediated *de novo* DNA methylation [236, 237], essential for orchestrating mammalian embryonic development [238]. Upregulation of *Sall3* in all $Dnmt1^{RES}$ germ layers may have also contributed to lineage-specific effects. In human induced pluripotent stem cells, SALL3 serves as a predictive marker for differentiation propensity, positively correlating with ectoderm and negatively with endoderm/mesoderm, mechanistically via modulation of DNMT3B function [239], another vital *de novo* DNA methyltransferase [238]. Gene expression regulation may have been supported by *Sall3* upregulation in $Dnmt1^{RES}$ ectoderm, while being hindered in $Dnmt1^{RES}$ endoderm and mesoderm. Additionally, sex chromosome genes were notably upregulated among $Dnmt1^{RES}$ cell types:

X-linked *Xlr3a-b/4b* in mESCs and ectoderm, *Xlr4a* in mESCs, endoderm, and ectoderm, and *Xlr3c/5a* in ectoderm, as well as Y-linked *Uty*, *Ddx3y*, and *Eif2s3y* in all cell types, and *Kdm5d* in all three germ layers. The upregulation of X- and Y-linked genes aligns with sex chromosomes being significantly susceptible to permanent DNA hypomethylation in mESCs following transient *Dnmt1* inactivation. Collectively, these findings relate to how epigenetic perturbations can often have differential consequences based on cell type [20–22], with further distinctions due to sex-specific effects [11, 23].

Repercussions of epigenetic perturbations during embryonic development

In this study, the severe growth delay and morphological abnormalities of mouse embryoid bodies resulting from DNMT1 deficiency bared strong resemblance to the phenotypes of DNMT1-deficient mouse embryos, which die by mid-gestation, stunted and deformed [61]. Despite partial growth recovery, the persistent severe malformation of mouse embryoid bodies after rescuing DNMT1 post-differentiation suggests that such delayed intervention *in vivo*, at gastrulation or later developmental stages, would likely fail to avert the lethal embryonic outcomes of DNMT1 deficiency. An earlier rescue intervention during stages of greater cellular plasticity, such as the blastocyst stage where pluripotent stem cells are prominent, may better support embryo viability, as evidenced by the normal growth and morphology of embryoid bodies in which DNMT1 was rescued in mESCs before their differentiation. However, epigenetic perturbations can result in drastically worse effects *in vivo* than those observed *in vitro*. For instance, while DNMT1 overexpression in mESCs does not affect embryoid body growth and morphology [44], a similar level of overexpression causes mid-gestation lethality in mouse embryos [51], comparable to DNMT1 deficiency. Therefore, developmental defects may still emerge despite transient epigenetic perturbations only occurring in early stages of development. Indeed, significant developmental delays and a wide range of morphological anomalies were observed in the majority of mid-gestation mouse embryos lacking the DNMT1o protein [240]. DNMT1o is the oocyte-derived variant of DNMT1 that supports DNA methylation maintenance in mouse preimplantation embryos; DNMT1o deficiency permanently reduces DNA methylation levels in mouse embryos, especially at genomic imprints [241, 242]. DNMT1o-deficient mouse embryos thus exemplify transient epigenetic disruption during the early developmental stage of preimplantation, which precedes blastocyst formation. We previously demonstrated that DNMT1o deficiency during mouse embryonic development also impacts ExE tissues, causing their hyperplasia [243], possibly due to the dispensability of DNA methylation for their growth and survival [191]. Results from this study are consistent with those findings; the estimated proportion of ExE endoderm cells was significantly higher in DNMT1-deficient mouse embryoid bodies compared to controls. In contrast, rescuing DNMT1 in mESCs before the formation of embryoid bodies prevented this outcome, though whether ExE hyperplasia would be fully prevented *in vivo* remains an intriguing question. This could be explored by injecting the *Dnmt1*-rescue mESCs from this study into blastocyst-stage mouse embryos to gain deeper insights into how the repercussions of epigenetic perturbations may become intensified in the complex environment of embryonic development compared to *in vitro* models.

In conclusion, rescuing DNMT1 activity was insufficient to reverse the effects of its loss in mESCs; only partial reversal was achieved. Permanent effects were detected as well as effects triggered by the rescue intervention, highlighting the difficulty of completely reversing the impact of epigenetic perturbations without unintended consequences. The effects of transient loss of DNMT1 in mESCs extended well beyond DNA methylation alterations, encompassing broader molecular and cellular alterations. Disruption of histone modification landscapes and gene expression profiles were observed, along with transposable element derepression, genomic instability, as well as morphological and functional alterations, underscoring the far-reaching influence of DNMT1. Transient loss of DNMT1 in mESCs also enabled the discovery 20 regions with imprinted-like epigenetic and regulatory signatures, some of which may be relevant to human health. Finally, we demonstrated that rescuing DNMT1 activity after differentiation onset exacerbated molecular and cellular disturbances, enlightening the heightened sensitivity of differentiating cells to epigenetic perturbations and the favourability of intervening during stages of greater cellular plasticity. These findings broaden the scope and complexity of DNMT1-dependent mechanisms, emphasize the wide-ranging repercussions of modulating key epigenetic enzymes and provide insight into the potential and challenges of therapeutic interventions aimed at reversing the effects of epigenetic perturbations during embryonic development.

Limitations of the study

This study presents some limitations that warrant consideration. First, EM-seq does not distinguish 5-methylcytosine (5mC; methylation) from 5-hydroxymethylcytosine (5hmC; hydroxymethylation), an intermediate product of DNA demethylation by Ten-eleven translocation (TET) enzymes. However, given the low global 5hmC levels in mESCs (~3%) [244] and the stable expression of *Tet1-3* in our model, it is unlikely that 5hmC substantially skewed our results. Moreover, lack of parental single nucleotide polymorphisms in *Dnmt1*$^{tet/tet}$ mESCs prevented allele-specific profiling of epigenetic modifications and gene expression, thereby constraining the depth of our investigation into genomic imprinting maintenance. Additionally, male mESCs were chosen to avoid X inactivation effects and enable analysis of both sex chromosomes, therefore no sex-specific analyses were performed. However, considering that transient *Dnmt1* inactivation led to DNA hypomethylation of sex chromosomes in mESCs and dysregulation of X- and Y-linked genes in mESCs and upon their differentiation into germ layers, our understanding of sex-specific responses to epigenetic disruptions could be enhanced by additional experiments using a female *Dnmt1*$^{tet/tet}$ mESC model. Finally, alternative methods for inducing transient loss of DNMT1 in WT mESCs were not attempted, for example via DNMT1 inhibitors (e.g. 5-azacytidine [245], decitabine [246], and GSK-3484862 [246, 247]) or siRNA interference [248]. Compared to the Tet-Off system, these methods often exhibit poor reproducibility across entire cell populations, with some inhibitors also lacking DNMT specificity and having cytotoxic properties. The *Dnmt1*$^{tet/tet}$ model was therefore more suitable for a direct investigation of DNMT1-dependent mechanisms.

Acknowledgements

We thank the members of the McGraw laboratory for valuable insights and support throughout the course of this study, the McGill Genome Centre and *Génome Québec* for sequencing services, Ines Boufaied (Azrieli Research Centre of Sainte-Justine University Hospital) for assisting with FACS experiments, as well as Gregor Andelfinger (University of Montreal), and J. Richard Chaillet (University of Pittsburgh) for gifting R1 and *Dnmt1*$^{tet/tet}$ mESCs, respectively. The graphical abstract was created in BioRender: Dupas, T. (2025) https://BioRender.com/m42n953.

Author contributions: Conceptualization and methodology: E.E., S.M., V.B.-L., T.D., N.J-M.R., N.G., G.B., and D.S.; Investigation: E.E. and L.-M.L.; Formal analysis: E.E., A.L., and M.C.; Writing—original draft: E.E. and S.M.; Writing—review and editing: All authors; Visualization: E.E.; Supervision: S.M., G.B., and D.S.; Funding acquisition: S.M. and N.G.

Supplementary data

Supplementary data is available at NAR online.

Conflict of interest

None declared.

Funding

This work was supported by Natural Sciences and Engineering Research Council of Canada grants to S.M. (Grant numbers: RGPIN-2016-06232, RGPIN-2023-04559) and scholarship to E.E., a *Réseau Québecois en reproduction* grant to S.M. and N.G., a *Fonds de recherche du Québec – Santé* Junior 2 salary award to S.M and a *Fonds de recherche du Québec – Nature et Technologie* scholarship to E.E. Funding to pay the Open Access publication charges for this article was provided by the Natural Sciences and Engineering Research Council of Canada (Grant number: RGPIN-2023-04559).

Data availability

The Gene Expression Omnibus (GEO) accession number for raw and processed data produced in this study is GSE267053. The GEO accession numbers for published data utilized in this study are GSE123942 (*Zfp57* WT and KO mESCs) and GSE171749 (*Setdb1* WT and KO mESCs). Allele-specific methylated regions in mESCs (Leung 2014) and CpG methylation profiles of mouse sperm and oocytes (Wang 2014) are accessible via the UCSC table browser from the DNA methylation Track Hub. Single-cell RNA sequencing data used for deconvolution of embryoid body mRNA sequencing raw counts were obtained from the R package MouseGastrulationData v1.18.0. This study does not report original code. Scripts for data analysis can be provided upon request to lead contact.

References

1. Gibney ER, Nolan CM. Epigenetics and gene expression. *Heredity* 2010;**105**:4–13. https://doi.org/10.1038/hdy.2010.54
2. Jenuwein T, Allis CD. Translating the histone code. *Science* 2001;**293**:1074–80. https://doi.org/10.1126/science.1063127
3. Breton-Larrivée M, Elder E, McGraw S. DNA methylation, environmental exposures and early embryo development. *Anim Reprod* 2019;**16**:465–74. https://doi.org/10.21451/1984-3143-AR2019-0062
4. Li E. Chromatin modification and epigenetic reprogramming in mammalian development. *Nat Rev Genet* 2002;**3**:662–73. https://doi.org/10.1038/nrg887
5. Amstislavsky SY, Kizilova EA, Golubitsa AN *et al.* Preimplantation exposures of murine embryos to estradiol or methoxychlor change postnatal development. *Reprod Toxicol* 2004;**18**:103–8. https://doi.org/10.1016/j.reprotox.2003.10.008
6. Waring RH, Harris RM, Mitchell SC. In utero exposure to carcinogens: epigenetics, developmental disruption and consequences in later life. *Maturitas* 2016;**86**:59–63. https://doi.org/10.1016/j.maturitas.2016.01.008
7. Guan X, Chen X, Dai L *et al.* Low maternal dietary intake of choline regulates toll-like receptor 4 expression via histone H3K27me3 in fetal mouse neural progenitor cells. *Mol Nutr Food Res* 2021;**65**:e2000769. https://doi.org/10.1002/mnfr.202000769
8. Wang L, Chang S, Wang Z *et al.* Altered GNAS imprinting due to folic acid deficiency contributes to poor embryo development and may lead to neural tube defects. *Oncotarget* 2017;**8**:110797–810. https://doi.org/10.18632/oncotarget.22731
9. Krishnaveni GV, Veena SR, Karat SC *et al.* Association between maternal folate concentrations during pregnancy and insulin resistance in Indian children. *Diabetologia* 2014;**57**:110–21. https://doi.org/10.1007/s00125-013-3086-7
10. Legault LM, Bertrand-Lehouillier V, McGraw S. Pre-implantation alcohol exposure and developmental programming of FASD: an epigenetic perspective. *Biochem Cell Biol* 2018;**96**:117–30. https://doi.org/10.1139/bcb-2017-0141
11. Legault LM, Doiron K, Breton-Larrivée M *et al.* Pre-implantation alcohol exposure induces lasting sex-specific DNA methylation programming errors in the developing forebrain. *Clin Epigenet* 2021;**13**:164. https://doi.org/10.1186/s13148-021-01151-0
12. Portales-Casamar E, Lussier AA, Jones MJ *et al.* DNA methylation signature of human fetal alcohol spectrum disorder. *Epigenetics Chromatin* 2016;**9**:25. https://doi.org/10.1186/s13072-016-0074-4
13. Market-Velker BA, Fernandes AD, Mann MR. Side-by-side comparison of five commercial media systems in a mouse model: suboptimal *in vitro* culture interferes with imprint maintenance. *Biol Reprod* 2010;**83**:938–50. https://doi.org/10.1095/biolreprod.110.085480
14. White CR, Denomme MM, Tekpetey FR *et al.* High frequency of imprinted methylation errors in human preimplantation embryos. *Sci Rep* 2015;**5**:17311. https://doi.org/10.1038/srep17311
15. Whidden L, Martel J, Rahimi S *et al.* Compromised oocyte quality and assisted reproduction contribute to sex-specific effects on offspring outcomes and epigenetic patterning. *Hum Mol Genet* 2016;**25**:4649–60.
16. Choux C, Binquet C, Carmignac V *et al.* The epigenetic control of transposable elements and imprinted genes in newborns is affected by the mode of conception: ART versus spontaneous conception without underlying infertility. *Hum Reprod* 2018;**33**:331–40. https://doi.org/10.1093/humrep/dex366
17. Choufani S, Turinsky AL, Melamed N *et al.* Impact of assisted reproduction, infertility, sex and paternal factors on the placental DNA methylome. *Hum Mol Genet* 2019;**28**:372–85. https://doi.org/10.1093/hmg/ddy321
18. Alberry B, Laufer BI, Chater-Diehl E *et al.* Epigenetic impacts of early life stress in fetal alcohol spectrum disorders shape the neurodevelopmental continuum. *Front Mol Neurosci* 2021;**14**:671891. https://doi.org/10.3389/fnmol.2021.671891
19. Juruena MF, Gadelrab R, Cleare AJ *et al.* Epigenetics: a missing link between early life stress and depression. *Prog Neuropsychopharmacol Biol Psychiatry* 2021;**109**:110231. https://doi.org/10.1016/j.pnpbp.2020.110231
20. Rahman MF, McGowan PO. Cell-type-specific epigenetic effects of early life stress on the brain. *Transl Psychiatry* 2022;**12**:326. https://doi.org/10.1038/s41398-022-02076-9

21. Mews P, Van der Zee Y, Gurung A *et al.* Cell type–specific epigenetic priming of gene expression in nucleus accumbens by cocaine. *Sci Adv* 2024;**10**:eado3514. https://doi.org/10.1126/sciadv.ado3514
22. Lehle JD, McCarrey JR. Differential susceptibility to endocrine disruptor-induced epimutagenesis. *Environ Epigenet* 2020;**6**:dvaa016. https://doi.org/10.1093/eep/dvaa016
23. Svoboda LK, Ishikawa T, Dolinoy DC. Developmental toxicant exposures and sex-specific effects on epigenetic programming and cardiovascular health across generations. *Environmental Epigenetics* 2022;**8**:dvac017. https://doi.org/10.1093/eep/dvac017
24. Breton-Larrivée M, Elder E, Legault LM *et al.* Mitigating the detrimental developmental impact of early fetal alcohol exposure using a maternal methyl donor-enriched diet. *FASEB J* 2023;**37**:e22829. https://doi.org/10.1096/fj.202201564R
25. Wozniak JR, Fink BA, Fuglestad AJ *et al.* Four-year follow-up of a randomized controlled trial of choline for neurodevelopment in fetal alcohol spectrum disorder. *J Neurodevelop Disord* 2020;**12**:9. https://doi.org/10.1186/s11689-020-09312-7
26. Miranda Furtado CL, Dos Santos Luciano MC, Silva Santos RD *et al.* Epidrugs: targeting epigenetic marks in cancer treatment. *Epigenetics* 2019;**14**:1164–76. https://doi.org/10.1080/15592294.2019.1640546
27. Ong BX, Brunmeir R, Zhang Q *et al.* Regulation of thermogenic adipocyte differentiation and adaptive thermogenesis through histone acetylation. *Front Endocrinol* 2020;**11**:95. https://doi.org/10.3389/fendo.2020.00095
28. Park HS, Kim J, Ahn SH *et al.* Epigenetic targeting of histone deacetylases in diagnostics and treatment of depression. *Int J Mol Sci* 2021;**22**:5398. https://doi.org/10.3390/ijms22105398.
29. Shaffer B, McGraw S, Xiao SC *et al.* The DNMT1 intrinsically disordered domain regulates genomic methylation during development. *Genetics* 2015;**199**:533–41. https://doi.org/10.1534/genetics.114.173609
30. Pradhan S, Bacolla A, Wells RD *et al.* Recombinant human DNA (cytosine-5) methyltransferase. I. Expression, purification, and comparison of de novo and maintenance methylation. *J Biol Chem* 1999;**274**:33002–10. https://doi.org/10.1074/jbc.274.46.33002
31. Leonhardt H, Page AW, Weier HU *et al.* A targeting sequence directs DNA methyltransferase to sites of DNA replication in mammalian nuclei. *Cell* 1992;**71**:865–73. https://doi.org/10.1016/0092-8674(92)90561-P
32. Bashtrykov P, Jankevicius G, Smarandache A *et al.* Specificity of Dnmt1 for methylation of hemimethylated CpG sites resides in its catalytic domain. *Chem Biol* 2012;**19**:572–8. https://doi.org/10.1016/j.chembiol.2012.03.010
33. Kim M, Costello J. DNA methylation: an epigenetic mark of cellular memory. *Exp Mol Med* 2017;**49**:e322. https://doi.org/10.1038/emm.2017.10
34. Mortusewicz O, Schermelleh L, Walter J *et al.* Recruitment of DNA methyltransferase I to DNA repair sites. *Proc Natl Acad Sci USA* 2005;**102**:8905–9. https://doi.org/10.1073/pnas.0501034102
35. Hirasawa R, Chiba H, Kaneda M *et al.* Maternal and zygotic Dnmt1 are necessary and sufficient for the maintenance of DNA methylation imprints during preimplantation development. *Genes Dev* 2008;**22**:1607–16. https://doi.org/10.1101/gad.1667008
36. Borowczyk E, Mohan KN, D'Aiuto L *et al.* Identification of a region of the DNMT1 methyltransferase that regulates the maintenance of genomic imprints. *Proc Natl Acad Sci USA* 2009;**106**:20806–11. https://doi.org/10.1073/pnas.0905668106
37. McGraw S, Zhang JX, Farag M *et al.* Transient DNMT1 suppression reveals hidden heritable marks in the genome. *Nucleic Acids Res* 2015;**43**:1485–97. https://doi.org/10.1093/nar/gku1386
38. Li SY, Park J, Guan Y *et al.* DNMT1 in Six2 progenitor cells is essential for transposable element silencing and kidney development. *JASN* 2019;**30**:594–609. https://doi.org/10.1681/ASN.2018070687
39. Min B, Park JS, Jeong YS *et al.* Dnmt1 binds and represses genomic retroelements via DNA methylation in mouse early embryos. *Nucleic Acids Res* 2020;**48**:8431–44. https://doi.org/10.1093/nar/gkaa584
40. Davis KN, Qu PP, Ma S *et al.* Mutations in human DNA methyltransferase DNMT1 induce specific genome-wide epigenomic and transcriptomic changes in neurodevelopment. *Hum Mol Genet* 2023;**32**:3105–20. https://doi.org/10.1093/hmg/ddad123
41. Liu R, Kim KY, Jung YW *et al.* Dnmt1 regulates the myogenic lineage specification of muscle stem cells. *Sci Rep* 2016;**6**:35355. https://doi.org/10.1038/srep35355
42. Lee PP, Fitzpatrick DR, Beard C *et al.* A critical role for Dnmt1 and DNA methylation in T cell development, function, and survival. *Immunity* 2001;**15**:763–74. https://doi.org/10.1016/S1074-7613(01)00227-8
43. Londoño Gentile T, Lu C, Lodato PM *et al.* DNMT1 is regulated by ATP-citrate lyase and maintains methylation patterns during adipocyte differentiation. *Mol Cell Biol* 2013;**33**:3864–78. https://doi.org/10.1128/MCB.01495-12
44. D'Aiuto L, Di Maio R, Mohan KN *et al.* Mouse ES cells overexpressing DNMT1 produce abnormal neurons with upregulated NMDA/NR1 subunit. *Differentiation* 2011;**82**:9–17. https://doi.org/10.1016/j.diff.2011.03.003
45. Liu Y, Sun L, Jost JP. In differentiating mouse myoblasts DNA methyltransferase is posttranscriptionally and posttranslationally regulated. *Nucleic Acids Res* 1996;**24**:2718–22. https://doi.org/10.1093/nar/24.14.2718
46. Singh RP, Shiue K, Schomberg D *et al.* Cellular epigenetic modifications of neural stem cell differentiation. *Cell Transplant* 2009;**18**:1197–211. https://doi.org/10.3727/096368909X12483162197204
47. Sen GL, Reuter JA, Webster DE *et al.* DNMT1 maintains progenitor function in self-renewing somatic tissue. *Nature* 2010;**463**:563–7. https://doi.org/10.1038/nature08683
48. Liao J, Karnik R, Gu H *et al.* Targeted disruption of DNMT1, DNMT3A and DNMT3B in human embryonic stem cells. *Nat Genet* 2015;**47**:469–78. https://doi.org/10.1038/ng.3258
49. Li Z, Dai H, Martos SN *et al.* Distinct roles of DNMT1-dependent and DNMT1-independent methylation patterns in the genome of mouse embryonic stem cells. *Genome Biol* 2015;**16**:115. https://doi.org/10.1186/s13059-015-0685-2
50. Dahlet T, Argüeso Lleida A, Al Adhami H *et al.* Genome-wide analysis in the mouse embryo reveals the importance of DNA methylation for transcription integrity. *Nat Commun* 2020;**11**:3153. https://doi.org/10.1038/s41467-020-16919-w
51. Biniszkiewicz D, Gribnau J, Ramsahoye B *et al.* Dnmt1 overexpression causes genomic hypermethylation, loss of imprinting, and embryonic lethality. *Mol Cell Biol* 2002;**22**:2124–35. https://doi.org/10.1128/MCB.22.7.2124-2135.2002
52. Li B, Zhao J, Ma JX *et al.* Overexpression of DNMT1 leads to hypermethylation of H19 promoter and inhibition of Erk signaling pathway in disuse osteoporosis. *Bone* 2018;**111**:82–91. https://doi.org/10.1016/j.bone.2018.03.017
53. Hong L, Sun G, Peng L *et al.* The interaction between miR-148a and DNMT1 suppresses cell migration and invasion by reactivating tumor suppressor genes in pancreatic cancer. *Oncol Rep* 2018;**40**:2916–25. https://doi.org/10.3892/or.2018.6700
54. Peng W, Feng H, Pang L *et al.* Downregulation of CAMK2N1 due to DNA hypermethylation mediated by DNMT1 that promotes the progression of prostate cancer. *J Oncol* 2023;**2023**:4539045. https://doi.org/10.1155/2023/4539045
55. Symmank J, Bayer C, Schmidt C *et al.* DNMT1 modulates interneuron morphology by regulating Pak6 expression through

crosstalk with histone modifications. *Epigenetics* 2018;**13**:536–56. https://doi.org/10.1080/15592294.2018.1475980
56. Clements EG, Mohammad HP, Leadem BR *et al.* DNMT1 modulates gene expression without its catalytic activity partially through its interactions with histone-modifying enzymes. *Nucleic Acids Res* 2012;**40**:4334–46. https://doi.org/10.1093/nar/gks031
57. Jiang H, Cao HJ, Ma N *et al.* Chromatin remodeling factor ARID2 suppresses hepatocellular carcinoma metastasis via DNMT1-Snail axis. *Proc Natl Acad Sci USA* 2020;**117**:4770–80. https://doi.org/10.1073/pnas.1914937117
58. Merry CR, Forrest ME, Sabers JN *et al.* DNMT1-associated long non-coding RNAs regulate global gene expression and DNA methylation in colon cancer. *Hum Mol Genet* 2015;**24**:6240–53. https://doi.org/10.1093/hmg/ddv343
59. Mohan KN. DNMT1: catalytic and non-catalytic roles in different biological processes. *Epigenomics* 2022;**14**:629–43. https://doi.org/10.2217/epi-2022-0035
60. Espada J. Non-catalytic functions of DNMT1. *Epigenetics* 2012;**7**:115–8. https://doi.org/10.4161/epi.7.2.18756
61. Li E, Bestor TH, Jaenisch R. Targeted mutation of the DNA methyltransferase gene results in embryonic lethality. *Cell* 1992;**69**:915–26. https://doi.org/10.1016/0092-8674(92)90611-F
62. Dagar V, Hutchison W, Muscat A *et al.* Genetic variation affecting DNA methylation and the human imprinting disorder, Beckwith–Wiedemann syndrome. *Clin Epigenet* 2018;**10**:114. https://doi.org/10.1186/s13148-018-0546-4
63. Zhang Y, Chen FQ, Sun YH *et al.* Effects of DNMT1 silencing on malignant phenotype and methylated gene expression in cervical cancer cells. *J Exp Clin Cancer Res* 2011;**30**:98. https://doi.org/10.1186/1756-9966-30-98
64. Lin RK, Wu CY, Chang JW *et al.* Dysregulation of p53/Sp1 control leads to DNA methyltransferase-1 overexpression in lung cancer. *Cancer Res* 2010;**70**:5807–17. https://doi.org/10.1158/0008-5472.CAN-09-4161
65. Grayson DR, Jia X, Chen Y *et al.* Reelin promoter hypermethylation in schizophrenia. *Proc Natl Acad Sci USA* 2005;**102**:9341–6. https://doi.org/10.1073/pnas.0503736102
66. Ruzicka WB, Zhubi A, Veldic M *et al.* Selective epigenetic alteration of layer I GABAergic neurons isolated from prefrontal cortex of schizophrenia patients using laser-assisted microdissection. *Mol Psychiatry* 2007;**12**:385–97. https://doi.org/10.1038/sj.mp.4001954
67. Klein CJ, Botuyan MV, Wu Y *et al.* Mutations in DNMT1 cause hereditary sensory neuropathy with dementia and hearing loss. *Nat Genet* 2011;**43**:595–600. https://doi.org/10.1038/ng.830
68. Winkelmann J, Lin L, Schormair B *et al.* Mutations in DNMT1 cause autosomal dominant cerebellar ataxia, deafness and narcolepsy. *Hum Mol Genet* 2012;**21**:2205–10. https://doi.org/10.1093/hmg/dds035
69. Kondo N, Tohnai G, Sahashi K *et al.* DNA methylation inhibitor attenuates polyglutamine-induced neurodegeneration by regulating Hes5. *EMBO Mol Med* 2019;**11**. https://doi.org/10.15252/emmm.201708547
70. Singh V, Sharma P, Capalash N. DNA methyltransferase-1 inhibitors as epigenetic therapy for cancer. *CCDT* 2013;**13**:379–99. https://doi.org/10.2174/15680096113139990077
71. Mahmood N, Rabbani SA. Targeting DNA hypomethylation in malignancy by epigenetic therapies. *Adv Exp Med Biol* 2019;**1164**:179–96. https://doi.org/10.1007/978-3-030-22254-3_14
72. Do Carmo S, Hanzel CE, Jacobs ML *et al.* Rescue of Early bace-1 and global DNA demethylation by S-adenosylmethionine reduces amyloid pathology and improves cognition in an Alzheimer's model. *Sci Rep* 2016;**6**:34051. https://doi.org/10.1038/srep34051
73. Ohbo K, Tomizawa S. Epigenetic regulation in stem cell development, cell fate conversion, and reprogramming. *Biomol Concepts* 2015;**6**:1–9. https://doi.org/10.1515/bmc-2014-0036
74. Morey L, Santanach A, Di Croce L. Pluripotency and epigenetic factors in mouse embryonic stem cell fate regulation. *Mol Cell Biol* 2015;**35**:2716–28. https://doi.org/10.1128/MCB.00266-15
75. Vougiouklakis T, Nakamura Y, Saloura V. Critical roles of protein methyltransferases and demethylases in the regulation of embryonic stem cell fate. *Epigenetics* 2017;**12**:1015–27. https://doi.org/10.1080/15592294.2017.1391430
76. Tsumura A, Hayakawa T, Kumaki Y *et al.* Maintenance of self-renewal ability of mouse embryonic stem cells in the absence of DNA methyltransferases Dnmt1, Dnmt3a and Dnmt3b. *Genes Cells* 2006;**11**:805–14. https://doi.org/10.1111/j.1365-2443.2006.00984.x
77. Malla S, Kumari K, García-Prieto CA *et al.* The scaffolding function of LSD1 controls DNA methylation in mouse ESCs. *Nat Commun* 2024;**15**:7758. https://doi.org/10.1038/s41467-024-51966-7
78. Wang B, Zhu S, Deng Y *et al.* Establishment of a CRISPR/Cas9-mediated GATAD2B homozygous knockout human embryonic stem cell line. *Stem Cell Res* 2021;**57**:102590. https://doi.org/10.1016/j.scr.2021.102590
79. Gossen M, Bujard H. Tight control of gene expression in mammalian cells by tetracycline-responsive promoters. *Proc Natl Acad Sci USA* 1992;**89**:5547–51. https://doi.org/10.1073/pnas.89.12.5547
80. Tanaka KF, Ahmari SE, Leonardo ED *et al.* Flexible accelerated STOP tetracycline operator-knockin (FAST): a versatile and efficient new gene modulating system. *Biol Psychiatry* 2010;**67**:770–3. https://doi.org/10.1016/j.biopsych.2009.12.020
81. Saxena S, Maroju PA, Choudhury S *et al.* Analysis of transcript levels of a few schizophrenia candidate genes in neurons from a transgenic mouse embryonic stem cell model overexpressing DNMT1. *Gene* 2020;**757**:144934. https://doi.org/10.1016/j.gene.2020.144934
82. MacDonald WA, Mann MRW. Epigenetic regulation of genomic imprinting from germ line to preimplantation. *Mol Reprod Devel* 2014;**81**:126–40. https://doi.org/10.1002/mrd.22220
83. Xie W, Barr CL, Kim A *et al.* Base-resolution analyses of sequence and parent-of-origin dependent DNA methylation in the mouse genome. *Cell* 2012;**148**:816–31. https://doi.org/10.1016/j.cell.2011.12.035
84. Maupetit-Méhouas S, Montibus B, Nury D *et al.* Imprinting control regions (ICRs) are marked by mono-allelic bivalent chromatin when transcriptionally inactive. *Nucleic Acids Res* 2016;**44**:621–35. https://doi.org/10.1093/nar/gkv960
85. Proudhon C, Duffié R, Ajjan S *et al.* Protection against *de novo* methylation is instrumental in maintaining parent-of-origin methylation inherited from the gametes. *Mol Cell* 2012;**47**:909–20. https://doi.org/10.1016/j.molcel.2012.07.010
86. Strogantsev R, Krueger F, Yamazawa K *et al.* Allele-specific binding of ZFP57 in the epigenetic regulation of imprinted and non-imprinted monoallelic expression. *Genome Biol* 2015;**16**:112. https://doi.org/10.1186/s13059-015-0672-7
87. Duffié R, Ajjan S, Greenberg MV *et al.* The Gpr1/Zdbf2 locus provides new paradigms for transient and dynamic genomic imprinting in mammals. *Genes Dev* 2014;**28**:463–78. https://doi.org/10.1101/gad.232058.113
88. Thorvaldsen JL, Mann MR, Nwoko O *et al.* Analysis of sequence upstream of the endogenous H19 gene reveals elements both essential and dispensable for imprinting. *Mol Cell Biol* 2002;**22**:2450–62. https://doi.org/10.1128/MCB.22.8.2450-2462.2002
89. Yoon BJ, Herman H, Sikora A *et al.* Regulation of DNA methylation of Rasgrf1. *Nat Genet* 2002;**30**:92–6. https://doi.org/10.1038/ng795
90. Lin SP, Youngson N, Takada S *et al.* Asymmetric regulation of imprinting on the maternal and paternal chromosomes at the

Dlk1–Gtl2 imprinted cluster on mouse chromosome 12. *Nat Genet* 2003;**35**:97–102. https://doi.org/10.1038/ng1233
91. Hiura H, Sugawara A, Ogawa H *et al.* A tripartite paternally methylated region within the Gpr1–Zdbf2 imprinted domain on mouse chromosome 1 identified by meDIP-on-chip. *Nucleic Acids Res* 2014;**42**:10869. https://doi.org/10.1093/nar/gku624
92. Wood AJ, Roberts RG, Monk D *et al.* A screen for retrotransposed imprinted genes reveals an association between X chromosome homology and maternal germ-line methylation. *PLoS Genet* 2007;**3**:e20. https://doi.org/10.1371/journal.pgen.0030020
93. Evans HK, Weidman JR, Cowley DO *et al.* Comparative phylogenetic analysis of Blcap/Nnat reveals eutherian-specific imprinted gene. *Mol Biol Evol* 2005;**22**:1740–8. https://doi.org/10.1093/molbev/msi165
94. Williamson CM, Turner MD, Ball ST *et al.* Identification of an imprinting control region affecting the expression of all transcripts in the Gnas cluster. *Nat Genet* 2006;**38**:350–5. https://doi.org/10.1038/ng1731
95. Ono R, Shiura H, Aburatani H *et al.* Identification of a large novel imprinted gene cluster on mouse proximal chromosome 6. *Genome Res* 2003;**13**:1696–705. https://doi.org/10.1101/gr.906803
96. Lucifero D, Mertineit C, Clarke HJ *et al.* Methylation dynamics of imprinted genes in mouse germ cells. *Genomics* 2002;**79**:530–8. https://doi.org/10.1006/geno.2002.6732
97. Kim J, Ekram MB, Kim H *et al.* Imprinting control region (ICR) of the Peg3 domain. *Hum Mol Genet* 2012;**21**:2677–87. https://doi.org/10.1093/hmg/dds092
98. Yang T, Adamson TE, Resnick JL *et al.* A mouse model for Prader-Willi syndrome imprinting-centre mutations. *Nat Genet* 1998;**19**:25–31. https://doi.org/10.1038/ng0598-25
99. Fitzpatrick GV, Soloway PD, Higgins MJ. Regional loss of imprinting and growth deficiency in mice with a targeted deletion of KvDMR1. *Nat Genet* 2002;**32**:426–31. https://doi.org/10.1038/ng988
100. Arima T, Wake N. Establishment of the primary imprint of the HYMAI/PLAGL1 imprint control region during oogenesis. *Cytogenet Genome Res* 2006;**113**:247–52. https://doi.org/10.1159/000090839
101. Zhang Z, Joh K, Yatsuki H *et al.* Comparative analyses of genomic imprinting and CpG island-methylation in mouse Murr1 and human MURR1 loci revealed a putative imprinting control region in mice. *Gene* 2006;**366**:77–86. https://doi.org/10.1016/j.gene.2005.08.020
102. Shiura H, Nakamura K, Hikichi T *et al.* Paternal deletion of Meg1/Grb10 DMR causes maternalization of the Meg1/Grb10 cluster in mouse proximal Chromosome 11 leading to severe pre- and postnatal growth retardation. *Hum Mol Genet* 2009;**18**:1424–38. https://doi.org/10.1093/hmg/ddp049
103. Wutz A, Smrzka OW, Schweifer N *et al.* Imprinted expression of the Igf2r gene depends on an intronic CpG island. *Nature* 1997;**389**:745–9. https://doi.org/10.1038/39631
104. Smith RJ, Dean W, Konfortova G *et al.* Identification of novel imprinted genes in a genome-wide screen for maternal methylation. *Genome Res* 2003;**13**:558–69. https://doi.org/10.1101/gr.781503
105. Okamura K, Wintle RF, Scherer SW. Characterization of the differentially methylated region of the Impactgene that exhibits Glires-specific imprinting. *Genome Biol* 2008;**9**:R160. https://doi.org/10.1186/gb-2008-9-11-r160
106. Song Q, Decato B, Hong EE *et al.* A reference methylome database and analysis pipeline to facilitate integrative and comparative epigenomics. *PLoS One* 2013;**8**:e81148. https://doi.org/10.1371/journal.pone.0081148
107. Leung D, Du T, Wagner U *et al.* Regulation of DNA methylation turnover at LTR retrotransposons and imprinted loci by the histone methyltransferase Setdb1. *Proc Natl Acad Sci USA* 2014;**111**:6690–5. https://doi.org/10.1073/pnas.1322273111
108. Karolchik D, Hinrichs AS, Furey TS *et al.* The UCSC Table Browser data retrieval tool. *Nucleic Acids Res* 2004;**32**:493D–496. https://doi.org/10.1093/nar/gkh103
109. Liao Y, Smyth GK, Shi W. The R package Rsubread is easier, faster, cheaper and better for alignment and quantification of RNA sequencing reads. *Nucleic Acids Res* 2019;**47**:e47. https://doi.org/10.1093/nar/gkz114
110. Cavalcante RG, Sartor MA. annotatr: genomic regions in context. *Bioinformatics* 2017;**33**:2381–3. https://doi.org/10.1093/bioinformatics/btx183
111. Abascal F, Acosta R, Addleman NJ *et al.* Expanded encyclopaedias of DNA elements in the human and mouse genomes. *Nature* 2020;**583**:699–710.
112. Bourgey M, Dali R, Eveleigh R *et al.* GenPipes: an open-source framework for distributed and scalable genomic analyses. *GigaScience* 2019;**8**:giz037. https://doi.org/10.1093/gigascience/giz037
113. Bolger AM, Lohse M, Usadel B. Trimmomatic: a flexible trimmer for Illumina sequence data. *Bioinformatics* 2014;**30**:2114–20. https://doi.org/10.1093/bioinformatics/btu170
114. Krueger F, Andrews SR. Bismark: A flexible aligner and methylation caller for Bisulfite-Seq applications. *Bioinformatics* 2011;**27**:1571–2. https://doi.org/10.1093/bioinformatics/btr167
115. Tarasov A, Vilella AJ, Cuppen E *et al.* Sambamba: fast processing of NGS alignment formats. *Bioinformatics* 2015;**31**:2032–4. https://doi.org/10.1093/bioinformatics/btv098
116. Li H, Durbin R. Fast and accurate short read alignment with Burrows–Wheeler transform. *Bioinformatics* 2009;**25**:1754–60. https://doi.org/10.1093/bioinformatics/btp324
117. Li H, Handsaker B, Wysoker A *et al.* The sequence alignment/map format and SAMtools. *Bioinformatics* 2009;**25**:2078–9. https://doi.org/10.1093/bioinformatics/btp352
118. Zhang Y, Liu T, Meyer CA *et al.* Model-based analysis of ChIP-Seq (MACS). *Genome Biol* 2008;**9**:R137. https://doi.org/10.1186/gb-2008-9-9-r137
119. Quinlan AR, Hall IM. BEDTools: a flexible suite of utilities for comparing genomic features. *Bioinformatics* 2010;**26**:841–2. https://doi.org/10.1093/bioinformatics/btq033
120. Tu S, Li M, Chen H *et al.* MAnorm2 for quantitatively comparing groups of ChIP-seq samples. *Genome Res* 2021;**31**:131–45. https://doi.org/10.1101/gr.262675.120
121. Gu Z, Eils R, Schlesner M. Complex heatmaps reveal patterns and correlations in multidimensional genomic data. *Bioinformatics* 2016;**32**:2847–9. https://doi.org/10.1093/bioinformatics/btw313
122. Gu Z, Eils R, Schlesner M *et al.* EnrichedHeatmap: an R/Bioconductor package for comprehensive visualization of genomic signal associations. *BMC Genomics* 2018;**19**:234. https://doi.org/10.1186/s12864-018-4625-x
123. Wang L, Zhang J, Duan J *et al.* Programming and inheritance of parental DNA methylomes in mammals. *Cell* 2014;**157**:979–91. https://doi.org/10.1016/j.cell.2014.04.017
124. Zheng R, Wan C, Mei S *et al.* Cistrome Data Browser: expanded datasets and new tools for gene regulatory analysis. *Nucleic Acids Res* 2019;**47**:D729–35. https://doi.org/10.1093/nar/gky1094
125. Takahashi N, Coluccio A, Thorball CW *et al.* ZNF445 is a primary regulator of genomic imprinting. *Genes Dev* 2019;**33**:49–54. https://doi.org/10.1101/gad.320069.118
126. Fornes O, Castro-Mondragon JA, Khan A *et al.* JASPAR 2020: update of the open-access database of transcription factor binding profiles. *Nucleic Acids Res* 2020;**48**:D87–92.
127. Bailey TL, Johnson J, Grant CE *et al.* The MEME Suite. *Nucleic Acids Res* 2015;**43**:W39–49. https://doi.org/10.1093/nar/gkv416
128. Dobin A, Davis CA, Schlesinger F *et al.* STAR: ultrafast universal RNA-seq aligner. *Bioinformatics* 2013;**29**:15–21. https://doi.org/10.1093/bioinformatics/bts635
129. Anders S, Pyl PT, Huber W. HTSeq–a Python framework to work with high-throughput sequencing data. *Bioinformatics* 2015;**31**:166–9. https://doi.org/10.1093/bioinformatics/btu638

130. Pertea M, Pertea GM, Antonescu CM *et al.* StringTie enables improved reconstruction of a transcriptome from RNA-seq reads. *Nat Biotechnol* 2015;**33**:290–5. https://doi.org/10.1038/nbt.3122
131. Love MI, Huber W, Anders S. Moderated estimation of fold change and dispersion for RNA-seq data with DESeq2. *Genome Biol* 2014;**15**:550. https://doi.org/10.1186/s13059-014-0550-8
132. Liao Y, Smyth GK, Shi W. featureCounts: an efficient general purpose program for assigning sequence reads to genomic features. *Bioinformatics* 2014;**30**:923–30. https://doi.org/10.1093/bioinformatics/btt656
133. Liao Y, Smyth GK, Shi W. The Subread aligner: fast, accurate and scalable read mapping by seed-and-vote. *Nucleic Acids Res* 2013;**41**:e108. https://doi.org/10.1093/nar/gkt214
134. Wu T, Hu E, Xu S *et al.* clusterProfiler 4.0: a universal enrichment tool for interpreting omics data. *Innovation (Camb)* 2021;**2**:100141.
135. Subramanian A, Tamayo P, Mootha VK *et al.* Gene set enrichment analysis: a knowledge-based approach for interpreting genome-wide expression profiles. *Proc Natl Acad Sci USA* 2005;**102**:15545–50. https://doi.org/10.1073/pnas.0506580102
136. Liberzon A, Birger C, Thorvaldsdóttir H *et al.* The Molecular Signatures Database (MSigDB) hallmark gene set collection. *Cell Syst* 2015;**1**:417–25. https://doi.org/10.1016/j.cels.2015.12.004
137. Hahne F, Ivanek R. In: Mathé E, Davis S (eds.), *Statistical Genomics: Methods and Protocols*. New York, NY: Springer New York, 2016, 335–51.
138. Ramírez F, Ryan DP, Grüning B *et al.* deepTools2: a next generation web server for deep-sequencing data analysis. *Nucleic Acids Res* 2016;**44**:W160–5. https://doi.org/10.1093/nar/gkw257
139. Shi H, Strogantsev R, Takahashi N *et al.* ZFP57 regulation of transposable elements and gene expression within and beyond imprinted domains. *Epigenetics Chromatin* 2019;**12**:49. https://doi.org/10.1186/s13072-019-0295-4
140. Barral A, Pozo G, Ducrot L *et al.* SETDB1/NSD-dependent H3K9me3/H3K36me3 dual heterochromatin maintains gene expression profiles by bookmarking poised enhancers. *Mol Cell* 2022;**82**:816–32. https://doi.org/10.1016/j.molcel.2021.12.037
141. Edgar R, Domrachev M, Lash AE. Gene Expression Omnibus: NCBI gene expression and hybridization array data repository. *Nucleic Acids Res* 2002;**30**:207–10. https://doi.org/10.1093/nar/30.1.207
142. Barrett T, Wilhite SE, Ledoux P *et al.* NCBI GEO: archive for functional genomics data sets–update. *Nucleic Acids Res* 2013;**41**:D991–5. https://doi.org/10.1093/nar/gks1193
143. Callicott RJ, Womack JE. Real-time PCR assay for measurement of mouse telomeres. *Comp Med* 2006;**56**:17–22.
144. Cawthon RM. Telomere measurement by quantitative PCR. *Nucleic Acids Res* 2002;**30**:47e–47. https://doi.org/10.1093/nar/30.10.e47
145. Livak KJ, Schmittgen TD. Analysis of relative gene expression data using real-time quantitative PCR and the 2(-Delta Delta C(T)) Method. *Methods* 2001;**25**:402–8. https://doi.org/10.1006/meth.2001.1262
146. Pijuan-Sala B, Griffiths JA, Guibentif C *et al.* A single-cell molecular map of mouse gastrulation and early organogenesis. *Nature* 2019;**566**:490–5. https://doi.org/10.1038/s41586-019-0933-9
147. Wang X, Park J, Susztak K *et al.* Bulk tissue cell type deconvolution with multi-subject single-cell expression reference. *Nat Commun* 2019;**10**:380. https://doi.org/10.1038/s41467-018-08023-x
148. Fan J, Lyu Y, Zhang Q *et al.* MuSiC2: cell-type deconvolution for multi-condition bulk RNA-seq data. *Brief Bioinf* 2022;**23**:bbac430. https://doi.org/10.1093/bib/bbac430
149. Meissner A, Gnirke A, Bell GW *et al.* Reduced representation bisulfite sequencing for comparative high-resolution DNA methylation analysis. *Nucleic Acids Res* 2005;**33**:5868–77. https://doi.org/10.1093/nar/gki901
150. Meissner A, Mikkelsen TS, Gu H *et al.* Genome-scale DNA methylation maps of pluripotent and differentiated cells. *Nature* 2008;**454**:766–70. https://doi.org/10.1038/nature07107
151. Smith ZD, Gu H, Bock C *et al.* High-throughput bisulfite sequencing in mammalian genomes. *Methods* 2009;**48**:226–32. https://doi.org/10.1016/j.ymeth.2009.05.003
152. Gu H, Smith ZD, Bock C *et al.* Preparation of reduced representation bisulfite sequencing libraries for genome-scale DNA methylation profiling. *Nat Protoc* 2011;**6**:468–81. https://doi.org/10.1038/nprot.2010.190
153. Orozco LD, Morselli M, Rubbi L *et al.* Epigenome-wide association of liver methylation patterns and complex metabolic traits in mice. *Cell Metab* 2015;**21**:905–17. https://doi.org/10.1016/j.cmet.2015.04.025
154. Bartolomei MS, Ferguson-Smith AC. Mammalian genomic imprinting. *Cold Spring Harb Perspect Biol* 2011;**3**:a002592. https://doi.org/10.1101/cshperspect.a002592
155. Elhamamsy AR. Role of DNA methylation in imprinting disorders: an updated review. *J Assist Reprod Genet* 2017;**34**:549–62. https://doi.org/10.1007/s10815-017-0895-5
156. Chiba H, Hiura H, Okae H *et al.* DNA methylation errors in imprinting disorders and assisted reproductive technology. *Pediatr Int* 2013;**55**:542–9. https://doi.org/10.1111/ped.12185
157. Quenneville S, Verde G, Corsinotti A *et al.* In embryonic stem cells, ZFP57/KAP1 recognize a methylated hexanucleotide to affect chromatin and DNA methylation of imprinting control regions. *Mol Cell* 2011;**44**:361–72. https://doi.org/10.1016/j.molcel.2011.08.032
158. Li X, Ito M, Zhou F *et al.* A maternal-zygotic effect gene, Zfp57, maintains both maternal and paternal imprints. *Dev Cell* 2008;**15**:547–57. https://doi.org/10.1016/j.devcel.2008.08.014
159. Yang H, Bai D, Li Y *et al.* Allele-specific H3K9me3 and DNA methylation co-marked CpG-rich regions serve as potential imprinting control regions in pre-implantation embryo. *Nat Cell Biol* 2022;**24**:783–92. https://doi.org/10.1038/s41556-022-00900-4
160. Jansz N. DNA methylation dynamics at transposable elements in mammals. *Essays Biochem* 2019;**63**:677–89.
161. Gebrie A. Transposable elements as essential elements in the control of gene expression. *Mobile DNA* 2023;**14**:9. https://doi.org/10.1186/s13100-023-00297-3
162. Bhat A, Ghatage T, Bhan S *et al.* Role of transposable elements in genome stability: implications for health and disease. *Int J Mol Sci* 2022;**23**:7802. https://doi.org/10.3390/ijms23147802
163. Fueyo R, Judd J, Feschotte C *et al.* Roles of transposable elements in the regulation of mammalian transcription. *Nat Rev Mol Cell Biol* 2022;**23**:481–97. https://doi.org/10.1038/s41580-022-00457-y
164. Kigami D, Minami N, Takayama H *et al.* MuERV-L is one of the earliest transcribed genes in mouse one-cell embryos. *Biol Reprod* 2003;**68**:651–4. https://doi.org/10.1095/biolreprod.102.007906
165. Evsikov AV, de Vries WN, Peaston AE *et al.* Systems biology of the 2-cell mouse embryo. *Cytogenet Genome Res* 2004;**105**:240–50. https://doi.org/10.1159/000078195
166. Peaston AE, Evsikov AV, Graber JH *et al.* Retrotransposons regulate host genes in mouse oocytes and preimplantation embryos. *Dev Cell* 2004;**7**:597–606. https://doi.org/10.1016/j.devcel.2004.09.004
167. Macfarlan TS, Gifford WD, Driscoll S *et al.* Embryonic stem cell potency fluctuates with endogenous retrovirus activity. *Nature* 2012;**487**:57–63. https://doi.org/10.1038/nature11244
168. Eckersley-Maslin MA, Svensson V, Krueger C *et al.* MERVL/Zscan4 network activation results in transient genome-wide DNA demethylation of mESCs. *Cell Rep* 2016;**17**:179–92. https://doi.org/10.1016/j.celrep.2016.08.087

169. Blasco MA. The epigenetic regulation of mammalian telomeres. *Nat Rev Genet* 2007;**8**:299–309. https://doi.org/10.1038/nrg2047
170. Buxton JL, Suderman M, Pappas JJ *et al.* Human leukocyte telomere length is associated with DNA methylation levels in multiple subtelomeric and imprinted loci. *Sci Rep* 2014;**4**:4954. https://doi.org/10.1038/srep04954
171. Dong Y, Huang Y, Gutin B *et al.* Associations between global DNA methylation and telomere length in healthy adolescents. *Sci Rep* 2017;**7**:4210. https://doi.org/10.1038/s41598-017-04493-z
172. Zalzman M, Falco G, Sharova LV *et al.* Zscan4 regulates telomere elongation and genomic stability in ES cells. *Nature* 2010;**464**:858–63. https://doi.org/10.1038/nature08882
173. Zhang Q, Dan J, Wang H *et al.* Tcstv1 and Tcstv3 elongate telomeres of mouse ES cells. *Sci Rep* 2016;**6**:19852. https://doi.org/10.1038/srep19852
174. Raefski AS, O'Neill MJ. Identification of a cluster of X-linked imprinted genes in mice. *Nat Genet* 2005;**37**:620–4. https://doi.org/10.1038/ng1567
175. Ben-Porath I, Thomson MW, Carey VJ *et al.* An embryonic stem cell-like gene expression signature in poorly differentiated aggressive human tumors. *Nat Genet* 2008;**40**:499–507. https://doi.org/10.1038/ng.127
176. Foster CT, Dovey OM, Lezina L *et al.* Lysine-specific demethylase 1 regulates the embryonic transcriptome and CoREST stability. *Mol Cell Biol* 2010;**30**:4851–63. https://doi.org/10.1128/MCB.00521-10
177. Macrae TA, Fothergill-Robinson J, Ramalho-Santos M. Regulation, functions and transmission of bivalent chromatin during mammalian development. *Nat Rev Mol Cell Biol* 2023;**24**:6–26. https://doi.org/10.1038/s41580-022-00518-2
178. Müller FJ, Laurent LC, Kostka D *et al.* Regulatory networks define phenotypic classes of human stem cell lines. *Nature* 2008;**455**:401–5. https://doi.org/10.1038/nature07213
179. Wong DJ, Liu H, Ridky TW *et al.* Module map of stem cell genes guides creation of epithelial cancer stem cells. *Cell Stem Cell* 2008;**2**:333–44. https://doi.org/10.1016/j.stem.2008.02.009
180. Pujana MA, Han JD, Starita LM *et al.* Network modeling links breast cancer susceptibility and centrosome dysfunction. *Nat Genet* 2007;**39**:1338–49. https://doi.org/10.1038/ng.2007.2
181. Leonard MO, Cottell DC, Godson C *et al.* The role of HIF-1 alpha in transcriptional regulation of the proximal tubular epithelial cell response to hypoxia. *J Biol Chem* 2003;**278**:40296–304. https://doi.org/10.1074/jbc.M302560200
182. Mense SM, Sengupta A, Zhou M *et al.* Gene expression profiling reveals the profound upregulation of hypoxia-responsive genes in primary human astrocytes. *Physiol Genomics* 2006;**25**:435–49. https://doi.org/10.1152/physiolgenomics.00315.2005
183. Elvidge GP, Glenny L, Appelhoff RJ *et al.* Concordant regulation of gene expression by hypoxia and 2-oxoglutarate-dependent dioxygenase inhibition: the role of HIF-1alpha, HIF-2alpha, and other pathways. *J Biol Chem* 2006;**281**:15215–26. https://doi.org/10.1074/jbc.M511408200
184. Winter SC, Buffa FM, Silva P *et al.* Relation of a hypoxia metagene derived from head and neck cancer to prognosis of multiple cancers. *Cancer Res* 2007;**67**:3441–9. https://doi.org/10.1158/0008-5472.CAN-06-3322
185. Qi J, Nakayama K, Cardiff RD *et al.* Siah2-dependent concerted activity of HIF and FoxA2 regulates formation of neuroendocrine phenotype and neuroendocrine prostate tumors. *Cancer Cell* 2010;**18**:23–38. https://doi.org/10.1016/j.ccr.2010.05.024
186. Rahe DP, Hobert O. Restriction of cellular plasticity of differentiated cells mediated by chromatin modifiers, transcription factors and protein kinases. *G3* 2019;**9**:2287–302. https://doi.org/10.1534/g3.119.400328
187. Pajerowski JD, Dahl KN, Zhong FL *et al.* Physical plasticity of the nucleus in stem cell differentiation. *Proc Natl Acad Sci USA* 2007;**104**:15619–24. https://doi.org/10.1073/pnas.0702576104
188. Brickman JM, Serup P. Properties of embryoid bodies. *WIREs Devel Biol* 2017;**6**:e259. https://doi.org/10.1002/wdev.259
189. Rhodes K, Barr KA, Popp JM *et al.* Human embryoid bodies as a novel system for genomic studies of functionally diverse cell types. *eLife* 2022;**11**:e71361. https://doi.org/10.7554/eLife.71361
190. Duval K, Grover H, Han L-H *et al.* Modeling physiological events in 2D vs. 3D cell culture. *Physiology* 2017;**32**:266–77. https://doi.org/10.1152/physiol.00036.2016
191. Sakaue M, Ohta H, Kumaki Y *et al.* DNA methylation is dispensable for the growth and survival of the extraembryonic lineages. *Curr Biol* 2010;**20**:1452–7. https://doi.org/10.1016/j.cub.2010.06.050
192. Verona RI, Thorvaldsen JL, Reese KJ *et al.* The transcriptional status but not the imprinting control region determines allele-specific histone modifications at the imprinted H19 locus. *Mol Cell Biol* 2008;**28**:71–82. https://doi.org/10.1128/MCB.01534-07
193. Sanz LA, Chamberlain S, Sabourin JC *et al.* A mono-allelic bivalent chromatin domain controls tissue-specific imprinting at Grb10. *EMBO J* 2008;**27**:2523–32. https://doi.org/10.1038/emboj.2008.142
194. Wang M, Chen Z, Zhang Y. CBP/p300 and HDAC activities regulate H3K27 acetylation dynamics and zygotic genome activation in mouse preimplantation embryos. *EMBO J* 2022;**41**:e112012. https://doi.org/10.15252/embj.2022112012
195. Voigt P, LeRoy G, Drury WJ 3rd *et al.* Asymmetrically modified nucleosomes. *Cell* 2012;**151**:181–93. https://doi.org/10.1016/j.cell.2012.09.002
196. Duncan IW. Transvection Effects in Drosophila. *Annu Rev Genet* 2002;**36**:521–56. https://doi.org/10.1146/annurev.genet.36.060402.100441
197. Tartof KD, Henikoff S. Trans-sensing effects from Drosophila to humans. *Cell* 1991;**65**:201–3. https://doi.org/10.1016/0092-8674(91)90153-P
198. Rassoulzadegan M, Magliano M, Cuzin F. Transvection effects involving DNA methylation during meiosis in the mouse. *Embo J* 2002;**21**:440–50. https://doi.org/10.1093/emboj/21.3.440
199. Liu H, Huang J, Wang J *et al.* Transvection mediated by the translocated cyclin D1 locus in mantle cell lymphoma. *J Exp Med* 2008;**205**:1843–58. https://doi.org/10.1084/jem.20072102
200. Creyghton MP, Cheng AW, Welstead GG *et al.* Histone H3K27ac separates active from poised enhancers and predicts developmental state. *Proc Natl Acad Sci USA* 2010;**107**:21931–6. https://doi.org/10.1073/pnas.1016071107
201. Kubo N, Chen PB, Hu R *et al.* H3K4me1 facilitates promoter-enhancer interactions and gene activation during embryonic stem cell differentiation. *Mol Cell* 2024; **84**:1742–52. https://doi.org/10.1016/j.molcel.2024.02.030
202. Rada-Iglesias A, Bajpai R, Swigut T *et al.* A unique chromatin signature uncovers early developmental enhancers in humans. *Nature* 2011;**470**:279–83. https://doi.org/10.1038/nature09692
203. Shlyueva D, Stampfel G, Stark A. Transcriptional enhancers: from properties to genome-wide predictions. *Nat Rev Genet* 2014;**15**:272–86. https://doi.org/10.1038/nrg3682
204. Tort F, Ferrer-Cortès X, Thió M *et al.* Mutations in the lipoyltransferase LIPT1 gene cause a fatal disease associated with a specific lipoylation defect of the 2-ketoacid dehydrogenase complexes. *Hum Mol Genet* 2014;**23**:1907–15. https://doi.org/10.1093/hmg/ddt585
205. Soreze Y, Boutron A, Habarou F *et al.* Mutations in human lipoyltransferase gene LIPT1 cause a Leigh disease with secondary deficiency for pyruvate and alpha-ketoglutarate dehydrogenase. *Orphanet J Rare Dis* 2013;**8**:192. https://doi.org/10.1186/1750-1172-8-192
206. Taché V, Bivina L, White S *et al.* Lipoyltransferase 1 gene defect resulting in fatal lactic acidosis in two siblings. *Case Rep Obstet Gynecol* 2016;**2016**:6520148. https://doi.org/10.1155/2016/6520148

207. Ni M, Solmonson A, Pan C *et al.* Functional assessment of lipoyltransferase-1 deficiency in cells, mice, and humans. *Cell Rep* 2019;**27**:1376–86. https://doi.org/10.1016/j.celrep.2019.04.005
208. Motta M, Fasano G, Gredy S *et al.* SPRED2 loss-of-function causes a recessive Noonan syndrome-like phenotype. *Am Hum Genet* 2021;**108**:2112–29. https://doi.org/10.1016/j.ajhg.2021.09.007
209. Abshagen K, Berger C, Dietrich A *et al.* A human REPIN1 gene variant: genetic risk factor for the development of nonalcoholic fatty liver disease. *Clin Transl Gastroenterol* 2020;**11**:e00114. https://doi.org/10.14309/ctg.0000000000000114
210. Lai W, Wu Y, Sha L *et al.* Identifying genetic factors of polycystic ovary syndrome in women with epilepsy: a whole-genome sequencing study. *Neuroendocrinology* 2024;**114**:223–33. https://doi.org/10.1159/000534531
211. Dibbens LM, Reid CA, Hodgson B *et al.* Augmented currents of an HCN2 variant in patients with febrile seizure syndromes. *Ann Neurol* 2010;**67**:542–6. https://doi.org/10.1002/ana.21909
212. DiFrancesco JC, Barbuti A, Milanesi R *et al.* Recessive loss-of-function mutation in the pacemaker HCN2 channel causing increased neuronal excitability in a patient with idiopathic generalized epilepsy. *J Neurosci* 2011;**31**:17327–37. https://doi.org/10.1523/JNEUROSCI.3727-11.2011
213. Nakamura Y, Shi X, Numata T *et al.* Novel HCN2 mutation contributes to febrile seizures by shifting the channel's kinetics in a temperature-dependent manner. *PLoS One* 2013;**8**:e80376. https://doi.org/10.1371/journal.pone.0080376
214. Li M, Maljevic S, Phillips AM *et al.* Gain-of-function HCN2 variants in genetic epilepsy. *Hum Mutat* 2018;**39**:202–9. https://doi.org/10.1002/humu.23357
215. Margolin DH, Kousi M, Chan YM *et al.* Ataxia, dementia, and hypogonadotropism caused by disordered ubiquitination. *N Engl J Med* 2013;**368**:1992–2003. https://doi.org/10.1056/NEJMoa1215993
216. Santens P, Van Damme T, Steyaert W *et al.* RNF216 mutations as a novel cause of autosomal recessive Huntington-like disorder. *Neurology* 2015;**84**:1760–6. https://doi.org/10.1212/WNL.0000000000001521
217. Esteves E, Mendes VM, Manadas B *et al.* COVID-19 salivary protein profile: unravelling molecular aspects of SARS-CoV-2 infection. *JCM* 2022;**11**:5571. https://doi.org/10.3390/jcm11195571
218. Chuang LS, Ian HI, Koh TW *et al.* Human DNA-(cytosine-5) methyltransferase-PCNA complex as a target for p21WAF1. *Science* 1997;**277**:1996–2000. https://doi.org/10.1126/science.277.5334.1996
219. Iida T, Suetake I, Tajima S *et al.* PCNA clamp facilitates action of DNA cytosine methyltransferase 1 on hemimethylated DNA. *Genes Cells* 2002;**7**:997–1007. https://doi.org/10.1046/j.1365-2443.2002.00584.x
220. Davies C, Brown CM, Westphal D *et al.* Murine norovirus replication induces G0/G1 cell cycle arrest in asynchronously growing cells. *J Virol* 2015;**89**:6057–66. https://doi.org/10.1128/JVI.03673-14
221. Xie J, Li B, Zhang P *et al.* Osteogenic protein-1 attenuates the inflammatory cytokine-induced NP cell senescence through regulating the ROS/NF-κB pathway. *Biomed Pharmacother* 2018;**99**:431–37. https://doi.org/10.1016/j.biopha.2018.01.053
222. Barra V, Schillaci T, Lentini L *et al.* Bypass of cell cycle arrest induced by transient DNMT1 post-transcriptional silencing triggers aneuploidy in human cells. *Cell Div* 2012;**7**:2. https://doi.org/10.1186/1747-1028-7-2
223. Sasatani M, Xu Y, Kawai H *et al.* RAD18 activates the G2/M checkpoint through DNA damage signaling to maintain genome integrity after ionizing radiation exposure. *PLoS One* 2015;**10**:e0117845. https://doi.org/10.1371/journal.pone.0117845
224. Selvarajah J, Elia A, Carroll VA *et al.* DNA damage-induced S and G2/M cell cycle arrest requires mTORC2-dependent regulation of Chk1. *Oncotarget* 2015;**6**:427–40. https://doi.org/10.18632/oncotarget.2813
225. Meyerson M, Harlow E. Identification of G1 kinase activity for cdk6, a novel cyclin D partner. *Mol Cell Biol* 1994;**14**:2077–86.
226. Lundberg AS, Weinberg RA. Functional inactivation of the retinoblastoma protein requires sequential modification by at least two distinct cyclin-cdk complexes. *Mol Cell Biol* 1998;**18**:753–61. https://doi.org/10.1128/MCB.18.2.753
227. Wang Z, Xie Y, Zhang L *et al.* Migratory localization of cyclin D2-Cdk4 complex suggests a spatial regulation of the G1-S transition. *Cell Struct Funct* 2008;**33**:171–83. https://doi.org/10.1247/csf.08019
228. Ando K, Ajchenbaum-Cymbalista F, Griffin JD. Regulation of G1/S transition by cyclins D2 and D3 in hematopoietic cells. *Proc Natl Acad Sci USA* 1993;**90**:9571–5. https://doi.org/10.1073/pnas.90.20.9571
229. Bennin DA, Don AS, Brake T *et al.* Cyclin G2 associates with protein phosphatase 2A catalytic and regulatory B' subunits in active complexes and induces nuclear aberrations and a G1/S phase cell cycle arrest. *J Biol Chem* 2002;**277**:27449–67. https://doi.org/10.1074/jbc.M111693200
230. Arachchige Don AS, Dallapiazza RF, Bennin DA *et al.* Cyclin G2 is a centrosome-associated nucleocytoplasmic shuttling protein that influences microtubule stability and induces a p53-dependent cell cycle arrest. *Exp Cell Res* 2006;**312**:4181–204. https://doi.org/10.1016/j.yexcr.2006.09.023
231. Le XF, Arachchige-Don AS, Mao W *et al.* Roles of human epidermal growth factor receptor 2, c-jun NH2-terminal kinase, phosphoinositide 3-kinase, and p70 S6 kinase pathways in regulation of cyclin G2 expression in human breast cancer cells. *Mol Cancer Ther* 2007;**6**:2843–57. https://doi.org/10.1158/1535-7163.MCT-07-0109
232. Zimmermann M, Arachchige-Don AS, Donaldson MS *et al.* Elevated cyclin G2 expression intersects with DNA damage checkpoint signaling and is required for a potent G2/M checkpoint arrest response to doxorubicin. *J Biol Chem* 2012;**287**:22838–53. https://doi.org/10.1074/jbc.M112.376855
233. de Lange T. Telomeres and senescence: ending the debate. *Science* 1998;**279**:334–5. https://doi.org/10.1126/science.279.5349.334
234. Bodnar AG, Ouellette M, Frolkis M *et al.* Extension of life-span by introduction of telomerase into normal human cells. *Science* 1998;**279**:349–52. https://doi.org/10.1126/science.279.5349.349
235. Rubio MA, Kim SH, Campisi J. Reversible manipulation of telomerase expression and telomere length. Implications for the ionizing radiation response and replicative senescence of human cells. *J Biol Chem* 2002;**277**:28609–17. https://doi.org/10.1074/jbc.M203747200
236. Holz-Schietinger C, Reich NO. The inherent processivity of the human *de novo* methyltransferase 3A (DNMT3A) is enhanced by DNMT3L. *J Biol Chem* 2010;**285**:29091–100. https://doi.org/10.1074/jbc.M110.142513
237. Veland N, Lu Y, Hardikar S *et al.* DNMT3L facilitates DNA methylation partly by maintaining DNMT3A stability in mouse embryonic stem cells. *Nucleic Acids Res* 2019;**47**:152–67. https://doi.org/10.1093/nar/gky947
238. Okano M, Bell DW, Haber DA *et al.* DNA methyltransferases Dnmt3a and Dnmt3b are essential for de novo methylation and mammalian development. *Cell* 1999;**99**:247–57. https://doi.org/10.1016/S0092-8674(00)81656-6
239. Kuroda T, Yasuda S, Tachi S *et al.* SALL3 expression balance underlies lineage biases in human induced pluripotent stem cell differentiation. *Nat Commun* 2019;**10**:2175. https://doi.org/10.1038/s41467-019-09511-4
240. Toppings M, Castro C, Mills PH *et al.* Profound phenotypic variation among mice deficient in the maintenance of genomic imprints. *Hum Reprod* 2008;**23**:807–18. https://doi.org/10.1093/humrep/den009
241. Carlson LL, Page AW, Bestor TH. Properties and localization of DNA methyltransferase in preimplantation mouse embryos:

implications for genomic imprinting. *Genes Dev* 1992;**6**:2536–41. https://doi.org/10.1101/gad.6.12b.2536
242. Mertineit C, Yoder JA, Taketo T *et al.* Sex-specific exons control DNA methyltransferase in mammalian germ cells. *Development* 1998;**125**:889–97. https://doi.org/10.1242/dev.125.5.889
243. McGraw S, Oakes CC, Martel J *et al.* Loss of DNMT1o disrupts imprinted X chromosome inactivation and accentuates placental defects in females. *PLoS Genet* 2013;**9**:e1003873. https://doi.org/10.1371/journal.pgen.1003873
244. Yan R, Cheng X, Gu C *et al.* Dynamics of DNA hydroxymethylation and methylation during mouse embryonic and germline development. *Nat Genet* 2023;**55**:130–43. https://doi.org/10.1038/s41588-022-01258-x
245. Patel K, Dickson J, Din S *et al.* Targeting of 5-aza-2′-deoxycytidine residues by chromatin-associated DNMT1 induces proteasomal degradation of the free enzyme. *Nucleic Acids Res* 2010;**38**:4313–24. https://doi.org/10.1093/nar/gkq187
246. Pappalardi MB, Keenan K, Cockerill M *et al.* Discovery of a first-in-class reversible DNMT1-selective inhibitor with improved tolerability and efficacy in acute myeloid leukemia. *Nat Cancer* 2021;**2**:1002–17. https://doi.org/10.1038/s43018-021-00249-x
247. Azevedo Portilho N, Saini D, Hossain I *et al.* The DNMT1 inhibitor GSK-3484862 mediates global demethylation in murine embryonic stem cells. *Epigenetics Chromatin* 2021;**14**:56.
248. Lai Q, Xu YH, Chen Q *et al.* The loss-of-function of DNA methyltransferase 1 by siRNA impairs the growth of non-small cell lung cancer with alleviated side effects via reactivation of RASSF1A and APC *in vitro* and *vivo*. *Oncotarget* 2017;**8**:59301–11. https://doi.org/10.18632/oncotarget.19573

Received: May 24, 2024. **Revised:** December 27, 2024. **Editorial Decision:** February 6, 2025. **Accepted:** February 11, 2025